

A survey of the solar data from the Murchison Widefield Array

A Thesis

submitted to

Indian Institute of Science Education and Research Pune

in partial fulfillment of the requirements for the

BS-MS Dual Degree Programme

by

Shilpi Bhunia



Indian Institute of Science Education and Research Pune

Dr. Homi Bhabha Road,
Pashan, Pune 411008, INDIA.

April, 2020

Supervisor: Dr. Divya Oberoi

© Shilpi Bhunia 2020

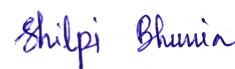
All rights reserved

Certificate

This is to certify that this dissertation entitled A survey of the solar data from the Murchison Widefield Array towards the partial fulfilment of the BS-MS dual degree programme at the Indian Institute of Science Education and Research, Pune represents study/work carried out by Shilpi Bhunia at Indian Institute of Science Education and Research under the supervision of Dr. Divya Oberoi, Reader, National Centre for Radio Astrophysics, during the academic year 2019-2020.



Dr. Divya Oberoi



Shilpi Bhunia

Committee:

Dr. Divya Oberoi

Prof. Prasad Subramanian

This thesis is dedicated to my parents.

Declaration

I hereby declare that the matter embodied in the report entitled A survey of the solar data from the Murchison Widefield Array are the results of the work carried out by me at the National Centre for Radio Astrophysics, Indian Institute of Science Education and Research, Pune, under the supervision of Dr. Divya Oberoi and the same has not been submitted elsewhere for any other degree.

Shilpi Bhunia

Shilpi Bhunia

Divya

Dr. Divya Oberoi

Acknowledgments

My deepest gratitude goes to my supervisor Dr. Divya Oberoi at National Centre for Radio Astrophysics. Throughout this project work, he has been very kind and patient with all my shortcomings. His office door was always open for me to ask him any doubts. I thank him for making me comfortable with coding. I do not think I could have found a better mentor for my thesis work. It has been an enjoyable experience working with him. I am also indebted to Aishwarya Thakur without him; it would not have been possible to make the query data tool.

I wish to express my thanks to Surajit Mondal ,and Devojjyoti Kansabanik, for their generous helps to my work.

My thanks go to Prof. Prasad Subramanian at the Indian Institute of Science Education and Research, Pune, for discussing with me about my doubts and giving me valuable suggestions.

I would also like to acknowledge the Indian Institute of Science Education and Research, Pune, and National Centre for Radio Astrophysics for giving me this tremendous opportunity.

My most profound appreciation goes to my friends for emotional support throughout this work.

Last but not least, I can not thank enough to my parents, who have sacrificed their entertainments just so my sister and I can be successful in our life.

Abstract

The Sun is a difficult radio source to study, but radio observations of the Sun carry crucial information about solar magnetic fields and coronal processes inaccessible by any other bands in the EM spectrum. Recently, instruments with capabilities matching the needs of solar radio physics have begun to become available. The Murchison Widefield Array (MWA), commissioned in mid-2013, is one such instrument which already has ~ 3000 hours of solar observations. Conventional radio interferometric imaging is very effort and computation intensive. As a part of building the ability to analyse large volumes of MWA data in an unsupervised manner, an automated imaging pipeline AIRCARS [8] has recently been developed. It routinely produces images with dynamic range between ~ 1000 to $\sim 100,000$, exceeding that of the earlier state of the art by two to three orders of magnitude. Along with the opportunity to strengthen our understanding of the Sun, every significant technological advance in solar observations has been accompanied by surprising new discoveries. This project aims to explore the potential of this newly acquired imaging capability. Given the very large computational burden of interferometric imaging, a key part of the problem is choosing the data to be analysed. This project explores a few different strategies for making this choice in an unbiased manner. We present the results from analysing some of the data so chosen using the imaging pipeline.

Contents

Abstract	vi
1 Basics of Interferometry	7
1.1 The Necessity of the Interferometry	7
1.2 Van Cittert Zernike Theorem	8
1.3 A Two Element Interferometer	9
1.4 Earth-Rotation Aperture Synthesis	12
2 Solar Locator of Observation Records for the MWA (SoLORM)	16
2.1 Sunspot Number (SSN) & 10.7 cm Radio Flux	17
2.2 Coronal Mass Ejection(CME) & Solar Flares	22
2.3 Geomagnetic Indices	25
2.4 Probing the MWA data	26
3 Imaging Process	29
3.1 Automated Imaging Routine for Compact Arrays for the Radio Sun (AIRCARS)	29
3.2 Flux Calibration	36
4 Type II Radio Burst: Results and Discussion	43

4.1	Dynamic Spectrum	44
4.2	Example of Solar Images	46
4.3	Analysis	47
5	Conclusion	64
5.1	Development of a tool for exploring MWA solar data - SoLORM	64
5.2	Analysis of type II solar burst	65
5.3	Results	66
5.4	Future Work	67

List of Figures

1	Different Emission mechanisms at different frequencies and height	4
1.1	Relationship between intensity and visibility	8
1.2	Schematic description of the interferometer	9
1.3	Plot of Voltage as a function of time	10
1.4	The trace of the interferometer when the source is at some angle from CNS .	12
1.5	The shape of the eclipse, traced by the interferometer	12
1.6	The trace of the interferometer at different declinations	13
1.7	The interferometer in 3 dimensions	14
2.1	The plot of SSN vs years	18
2.2	The plot of 10.7cm radio flux as a function of time.	19
2.3	A Schematic description of the code	19
2.4	The time series of daily sunspot numbers and F10.7 cm	20
2.5	A plot of daily sunspot numbers vs. solar flux 10.7	21
2.6	Histogram of slope values in the sunspot number and radio flux plane	21
2.7	Classification of flares	23
2.8	Histogram of total flare counts for full data set	23
2.9	Histogram of total CME counts for full data set	24

2.10	The CME and flare catalogues	24
2.11	The plot of Ap values as a function of date.	25
2.12	Histogram of MWA observations	27
3.1	The figure shows the point spread function of MWA.	32
3.2	The figure shows how the antennas are added for MWA	35
3.3	The improvement of the image quality because of the increase of the self-calibration iteration number.	35
3.4	The image of Virgo A with sun	37
3.5	The figure shows the region around VIRGO A, before and after CLEANing.	38
3.6	A plot of log(flux density) vs. log(frequency)	38
3.7	Power Pattern of an antenna ¹	39
3.8	The primary beam pattern of MWA.	40
3.9	Primary beam corrected image	40
3.10	The plot of attenuation factor as a function of frequency.	41
3.11	The plot shows how the scale factor changes with the frequencies.	41
4.1	An example of a type II burst	44
4.2	Dynamic spectrum of the type II burst in the Learmonth Spectrograph.	45
4.3	MWA dynamic spectrum and time series	45
4.4	Example of MWA solar images	46
4.5	Amplitude VS Time	48
4.6	RA shift and Dec shift using the auto color scale	53
4.7	RA shift and Dec shift using the same color scale	54
4.8	Visual representation of the RA shift and Dec shift	55

4.9	Visual representation of the RA shift and Dec shift 2	56
4.10	RA and Dec error	57
4.11	Peak of the fitted Gaussian amplitude	58
4.12	Major axis of the deconvolved image	59
4.13	Minor axis of the deconvolved image	60
4.14	PA of deconvolved image	61
4.15	major and minor axis in units of PSF.	62
4.16	PA difference between the fitted Gaussian	63

Introduction

The solar radio emissions are the signatures of all the incoherent and coherent processes happening in the different layers of the solar chromosphere, corona, and the heliosphere. Incoherent emissions include free-free emission and gyro-emission, coherent emission results from plasma processes.

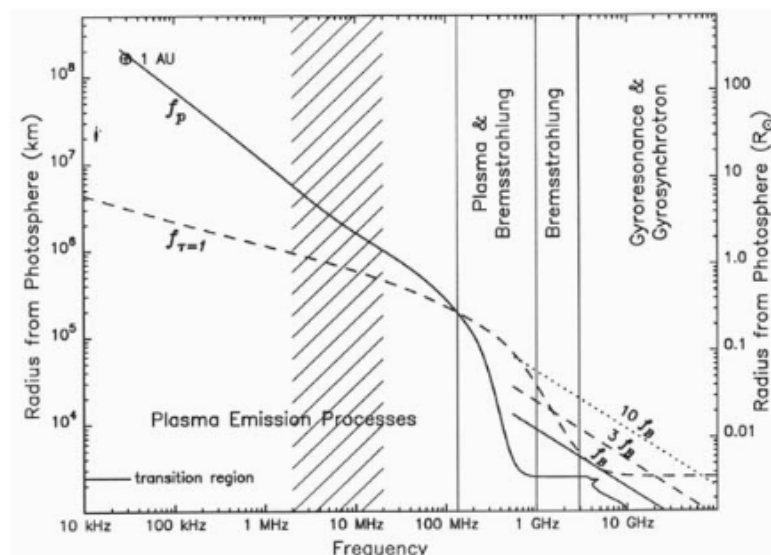


Figure 1: The figure describes the dominance of different emission mechanisms at different frequencies and heights [1].

- **Free-Free/Bremsstrahlung Emission** – This emission is produced when the electrons get accelerated due to the force exerted by the Coulomb field of the ambient ions. The free-free opacity is proportional to $\frac{n_e^2}{\nu^2 T^{3/2}}$, where n_e is the electron density along the line of sight. Consequently, the emission will become optically thick at low frequency, high density and low temperature. Hence, it will dominate at coronal

holes, quiet sun regions, prominences and sometimes at active regions.

- **Gyro-emission** – As the frequency increases, medium becomes optically thinner, the Bremsstrahlung emission become weaker and gyro-emission becomes the dominant emission. The emission is generated when the electrons gyrate around the magnetic field lines. The electron gyro frequency, $f_B = 2.8 \times 10^6 B$ Hz, where B is in Gauss. So we can also have an estimation of magnetic field if we have information about the frequency.
- **Plasma Emission** – When the non-thermal electrons get accelerated in the corona, it leads to a two-stream instability. This instability creates the plasma waves and a very tiny fraction of this energy is radiated as radio emission. The plasma frequency is, $f_p = 9000 \sqrt{n_e (cm^{-3})}$ Hz . This process produces the different well known types of radio bursts. In the outer corona, the plasma density decreases, yielding to the difficulty of the detection of the hard X ray and EUV emissions. In these regions, radio bursts provide essential diagnostics on the acceleration and propagation of the electrons during eruption events, leading to an overall better understanding of these events.

So these mechanisms are the reason we should look at the Sun in the radio regime.

According to the Rayleigh-Jeans law, the radio flux density (I_ν) is proportional to the brightness temperature. For the optical thick region, the brightness temperature is equal to the local electron temperature. Hence, often making the brightness temperature maps gives us a sense of the local temperature.

All these pieces of information about radio emission processes were already known. Some of these emission processes change over small temporal (<1 s) and spectral ($\lesssim 100$ KHz) periods. Hence to capture these changes, we need instruments with excellent spectral, angular, and temporal resolution, which was previously not feasible. This has recently been possible with the commissioning of new instruments. Murchison Widefield Array(MWA) is one such instrument with spectral resolution of 40 KHz and temporal resolution of 0.5 s. MWA data allows us to make an image of the Sun for every pixel in the dynamic spectrum. The imaging dynamic range of the MWA solar images spans the range from $\sim 10^3$ – 10^5 , which is well beyond the earlier state of the art. MWA images, hence, enables us to explore phase space which has been inaccessible till now with a spectroscopic imaging capability, which has already proven to be rewarding.

The first chapter describes the basics of the interferometry. The second chapter is about the aim and algorithm of Solar Locator of Observation Records for the MWA (SoLORM). The last two chapters are about the calibration process and analysis of the chosen data using SoLORM.

Chapter 1

Basics of Interferometry

The Murchison Widefield Array is a low-frequency radio array (80-300 MHz). As the MWA is an interferometer, before starting to work with MWA data, it is crucial to know the fundamentals of radio interferometry. This knowledge is essential for analysis of the data.

1.1 The Necessity of the Interferometry

We all know that the angular resolution of the antenna is given by

$$\theta \sim \frac{\lambda}{d} \tag{1.1}$$

where d is the aperture size and λ is the wavelength. To get a better resolution, we have two options - either decrease the wavelength or increase the aperture size. To have a better resolution, we can keep the telescopes restricted to observe at mm and cm wavelengths. But that will mean that we will only get to study the sources which produce brightest emissions at these wavelengths. But what about if we want to study some sources at meter wavelength. So, decreasing the wavelength is not a good choice. Hence we are only left with the second option. That also does not help that much. Because for example, if we have a 300m diameter of telescope which is observing at 1 meter wavelength, it can only have angular resolution of $\sim 10'$. Also telescope of this large size is also impossible to build. Hence the need for the interferometer, the principle of which is similar to the Young's

double-slit experiment. Like in the double-slit experiment, we can see fringes on the screen, similarly in the voltage output of the interferometer also these fringes can be seen.

1.2 Van Cittert Zernike Theorem

Let's assume that the slit separation in the double-slit experiment to be d . The visibility is defined as the contrast between maximum and minimum intensity. Decreasing the slit separation will lead to an increase in visibility. In Fig. 1.1, we can see for large source, the visibility falls off more quickly as d increases, which is not the case for the small sources.

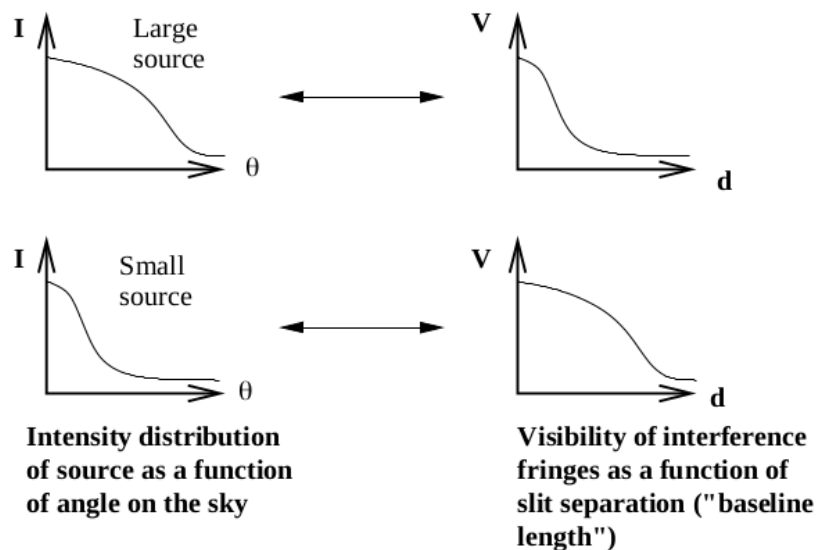


Figure 1.1: A description of the relationship between the intensity and the visibility. For small sources, visibility stays high for more larger slit separation than compare to the large sources[6].

Also, it is clearly evident that the correspondence between intensity and the visibility is a Fourier transform as it maps a broad Gaussian to a small Gaussian and the other way around. This relationship is called Van Cittert–Zernike theorem, which radio astronomers use extensively in radio interferometry[6].

1.3 A Two Element Interferometer

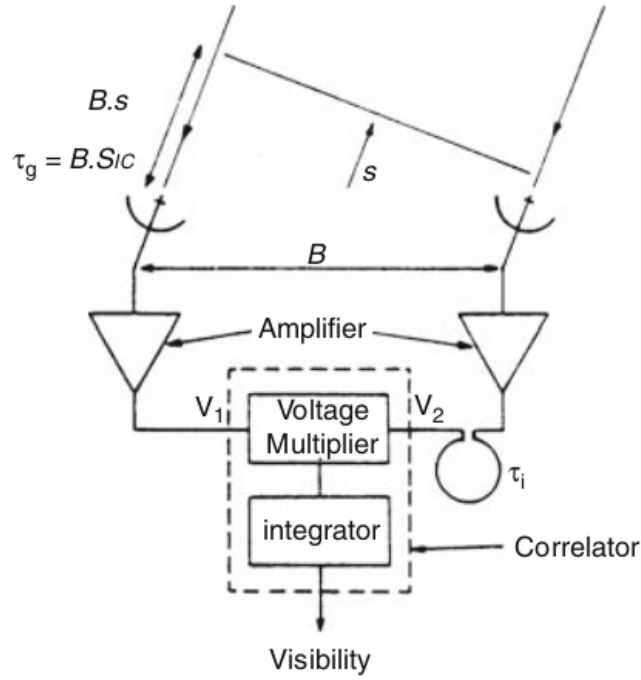


Figure 1.2: The figure gives a schematic description of the interferometer [9]. Here τ_g and τ_i correspond to the geometric and instrumental delay respectively.

In Fig.1.2, the interferometer has two antennas, which are separated by the baseline vector \vec{B} . Both of these antennas are looking at the point source of flux density S . If the electromagnetic wave coming from the point source is monochromatic and has frequency ν , then the voltage output at antenna 2 will be $V_2(t) = V \cos(\omega t)$. Now for the antenna 1, the wave has to travel extra distance $\vec{B} \cdot \vec{S}$. So the voltage output at the antenna 1 will be $V_1(t) = V \cos(\omega(t - \tau_g))$, where the geometric delay, $\tau_g = \vec{B} \cdot \vec{S} / c$. To get a correlator response, these two voltages first get multiplied and then get averaged. So the output is

$$R(\tau_g) \propto \frac{V^2}{T} \int_0^T \cos(\omega t) \cos(\omega(t - \tau_g)) dt \quad (1.2)$$

Considering the average time $T \gg (\omega)^{-1}$, we will get

$$R(\tau_g) = \frac{V^2}{2} \cos(\omega \tau_g) \quad (1.3)$$

If the effective area of each antenna is A , then $\frac{V^2}{2} \propto S_\nu A$.

τ_g is constant for only one direction. Since the Earth is rotating, τ_g will change and as a result we will get $R(\tau_g)$ as a function of time. We can see from Fig.1.3, that the instantaneous frequency of $R(\tau_g)$ will be maximum at zenith and minimum at the rising or setting of the source[4].

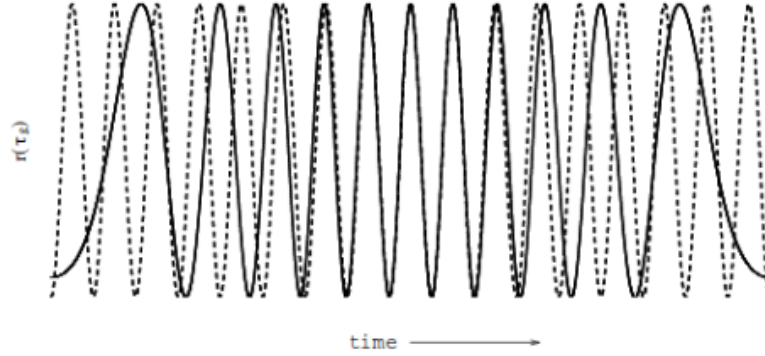


Figure 1.3: The output voltage as a function of time. The dotted line is a sinusoid whose frequency is equal to the maximum instantaneous frequency of the fringe. The instantaneous frequency will be maximum when the source will be at zenith and minimum when the source is rising or setting[4]

1.3.1 Finite Source Size

If we have source which has finite size and the sky brightness distribution of the source is $I(\vec{s})$, then we can think of the extended source as the sum of independent point sources. Then the output will be

$$R_e = \int A(\vec{s})I(\vec{s})\cos(\omega\tau_g)d\Omega \quad (1.4)$$

where $A(\vec{s})$ is the effective collecting area for each antenna. We can write $I = I_o + I_e$, where I_o and I_e are the odd and even part of the I . To detect I_o we need an odd function which we can get by introducing a phase delay of $\frac{\pi}{2}$ to the output of the antenna.

$$R_o = \int A(\vec{s})I(\vec{s})\sin(\omega\tau_g)d\Omega \quad (1.5)$$

Then we can get the complex visibility,

$$V = R_e - iR_o = \int A(\vec{s})I(\vec{s})exp(-i\omega\tau_g)d\Omega \quad (1.6)$$

1.3.2 Effects of Finite Bandwidth

Suppose a source emits quasi-monochromatic radiation and the radiation falls in bandwidth $\Delta\nu$ around some central frequency ν . Then, if we do the average over all the frequencies then the visibility will reduce. Because we know that the definition of the visibility is the difference between the maximum and minimum intensity and the summation of intensity distributions corresponding to different frequencies leads to the new intensity without any humps. Then Eq. 1.6 will become

$$V = \int \left[\int_{\nu-\Delta\nu/2}^{\nu+\Delta\nu/2} A(\vec{s})I(\vec{s}) \exp(-i2\pi\nu\tau_g) d\nu \right] d\Omega \quad (1.7)$$

If we consider that the intensity and the response of the interferometer do not change much over $\Delta\nu$, then we can write Eq.6 as

$$V \approx \int A(\vec{s})I(\vec{s})sinc(\Delta\nu\tau_g) \exp(-i2\pi\nu\tau_g)d\Omega \quad (1.8)$$

Here the attenuation factor is $sinc(\Delta\nu\tau_g)$. Clearly if the bandwidth increases, the visibility decreases. For the visibility to not decrease, we usually introduce a time delay τ_i in the signal path of the antenna 2 such that $|\tau_i - \tau_g| \ll \Delta\nu^{-1}$.

As τ_g varies if we change direction, we can only do delay compensation for only one direction.

The Bandwidth limit:

We know that $\tau_g = \frac{B \sin \theta}{c} = \frac{B\theta}{\lambda\nu} = \frac{\theta}{\theta_{res}\nu}$. So the condition for small attenuation

$$\begin{aligned} \frac{\Delta\nu\theta}{\nu\theta_{res}} &\ll 1 \\ \frac{\Delta\nu}{\nu} &\ll \frac{\theta_{beam}}{\Delta\theta} \end{aligned} \quad (1.9)$$

where $\frac{\Delta\nu}{\nu}$ and $\frac{\theta}{\theta_{res}}$ are respectively called fractional bandwidth and angular offset in

resolution unit.

One way we can have small attenuation that is to observe only over smaller bandwidth. But we need large bandwidth to have enough sensitivity, as the sensitivity is proportional to $(\Delta\nu)^{1/2}$. So what one can do is dividing the receiver into many independent neighbouring bands and have correlator system for each of these parts.

1.4 Earth-Rotation Aperture Synthesis

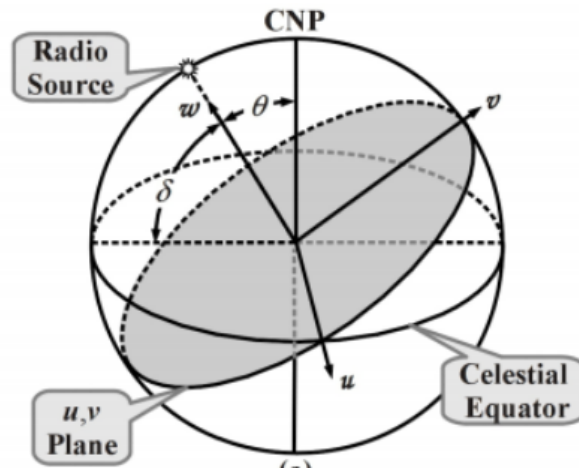


Figure 1.4: The source is at an angle θ from the Celestial North Pole. So the interferometer will trace out an eclipse[7]

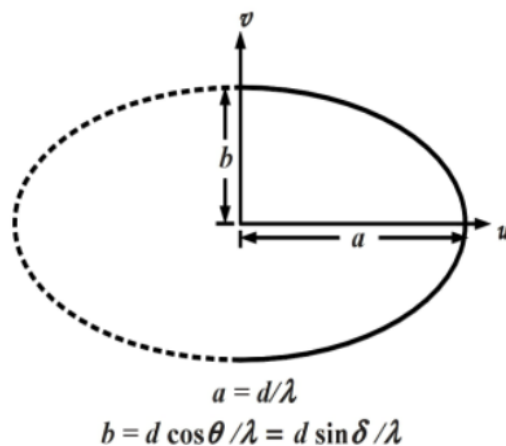


Figure 1.5: The minor axis, b is shortened by $\sin \delta$ where δ is the declination of the source[7].

If we have an interferometer with an East-West baseline, then the baseline will be parallel to the celestial equator. In Fig.1.4 the source is at an angle θ from the Celestial North Pole (CNP). Then in 24 hours the interferometer will trace out a complete eclipse on the (u,v) plane, where u and v are respectively the east-west and north-south part of the projected baseline of the interferometer in wavelengths. Let the baseline length be d, then the value of u will be b/λ and the value of v will be smaller by $\sin\delta$. It will look like Fig.1.5. If the source is at CNP, then the interferometer will trace a circle as δ becomes 90° . Also if the source is at the equator, it will trace a straight line[5][7].

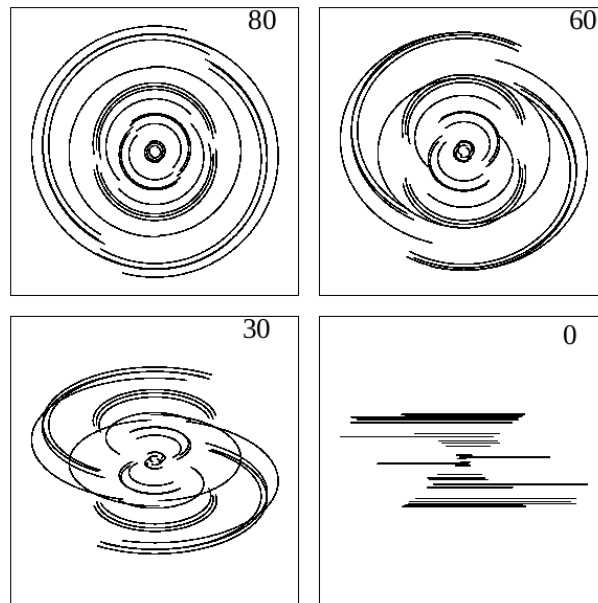


Figure 1.6: The traces of the interferometer in the u-v plane at different declinations- $80^\circ, 60^\circ, 30^\circ, 0^\circ$ [6]

1.4.1 Interferometers in 3 dimensions

Aperture synthesis is a technique used to obtain the intensity distribution of the source from a measured set of visibilities. In Fig.1.7, the coordinate system (u,v,w) has been introduced to describe the baseline in 3 dimensions. The w axis is pointing towards the direction of the target source \hat{s}_o . The (u,v) plane is normal to the w axis. Here, u,v,w are measured in the wavelength units. \hat{s} is the unit vector directed to any point on the source field from the centre of the source. Let's assume that \hat{s} has three components l,m,n, then

$n = \cos \theta = (1 - l^2 - m^2)^{1/2}$. Hence, we have the following equations

$$\vec{b} \cdot \hat{s} / \lambda = ul + vm + wn \quad (1.10)$$

$$d\Omega = \frac{dldm}{n} = \frac{dldm}{(1 - l^2 - m^2)^{1/2}} \quad (1.11)$$

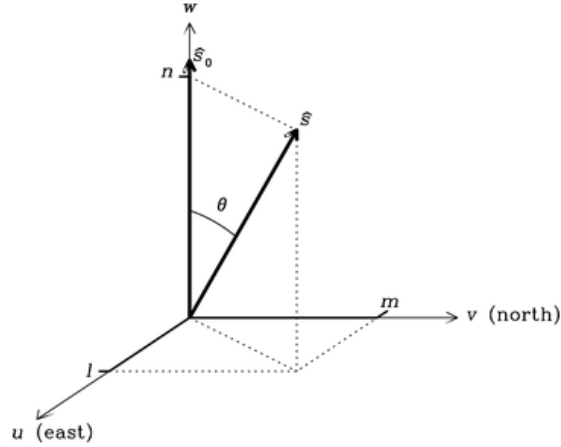


Figure 1.7: The interferometer in 3 dimensions. The w axis is pointing toward the phase center. The u and v are respectively the east-west and north-south component of the projected baseline of the interferometer in wavelengths[5].

Then Eq. 1.6 becomes,

$$V(u, v, w) = \int \int \frac{A(l, m)I(l, m)}{(1 - l^2 - m^2)^{1/2}} \exp[-i2\pi(ul + vm + wn)] dldm \quad (1.12)$$

Clearly the Eq. 1.12 is not a 3-d Fourier transform. In two cases, the equation becomes a Fourier transform.

1. When the array is perpendicular to \hat{s} , in other words if the $w = 0$, then we get

$$V(u, v) = \int \int \frac{A(l, m)I(l, m)}{(1 - l^2 - m^2)^{1/2}} \exp[-i2\pi(ul + vm)] dldm \quad (1.13)$$

2. If the source brightness distribution falls in a small region of the sky implying θ to be small, then we can write $n = \cos \theta = 1 - \frac{\theta^2}{2}$

$$V(u, v, w) \exp(-2\pi iw) = \int \int \frac{A(l, m)I(l, m)}{(1 - l^2 - m^2)^{1/2}} \exp[-i2\pi(ul + vm - w\theta^2/2)] dldm \quad (1.14)$$

we can write $\exp(-i2\pi w\theta^2/2) \approx 1$ for $w\theta^2 \ll 1$ implying small field of view for which $\theta \ll w^{-1/2}$, then we get

$$V(u, v, w)\exp(-i2\pi w) = \int \int \frac{A(l, m)I(l, m)}{(1 - l^2 - m^2)^{1/2}} \exp[-i2\pi(ul + vm)] dl dm \quad (1.15)$$

The factor $\exp(-i2\pi w)$ is required to do the conversion so that the antennas in the (u,v) plane can measure the visibility.

$$V(u, v, w)\exp(-i2\pi w) \cong V(u, v, 0) \quad (1.16)$$

Substituting Eq. 1.16 into 1.15 and doing the inverse Fourier transform we get,

$$I'(l, m) = A(l, m)I(l, m) = \int \int V(u, v, 0)\exp(-i2\pi(ul + vm)) du dv \quad (1.17)$$

We can correct $I'(l, m)$ by dividing by primary beam shape $A(l, m)$ [4][9][5].

Chapter 2

Solar Locator of Observation Records for the MWA (SoLORM)

Till now, MWA has observed the Sun for approximately 3000 hours. So it has very large quantities of data (a raw data rate of ~ 1 TB/hour). Hence to pick up an interesting data from these large dataset, first the user needs to know the various solar activities over the years. So that it will help the user to choose what they want to investigate. Keeping this in mind, we have built up a data tool ‘Solar Locator of Observation Records for the MWA’ (SoLORM).

We have chosen various parameters of interest for gauging the level of solar activity. The parameters are:

- Sunspot number
- 10.7 cm radio flux
- Coronal mass ejections (CMEs)
- Solar flares
- Geomagnetic indices (A_p & K_p)

The architecture of SoLORM has been developed in such a way that we first identify scientifically important dates and times by using established indicators of solar activity,

namely the Daily Sunspot Number and the 10.7 cm Radio Flux. Having thus identified a range of interest, we can then look for Flare and CME events in this range to narrow down a time frame of our interest. We then query the MWA observations database to check if observations are present for that time frame. SoLORM also returns a count of the number of MWA observations and the MWA observations data frame that match the conditions set by the user. Currently it uses sunspot number, 10.7 cm radio flux density, flares, CMEs and class of the flare for filtering the observations.

2.1 Sunspot Number (SSN) & 10.7 cm Radio Flux

- **Sunspot Number(SSN):** Sunspots are the dark spots on the solar photosphere, caused by the upliftment of the magnetic field flux in that area. The sun has a cycle of 11 years, where it goes through minima and maxima. Throughout the time of the solar minima, solar activity decreases, and few eruptive events happen in the sun. During solar maxima, the sun has the most number of sunspots. So the sunspot numbers can be used as an indicator of the solar activity.
For example, in Fig. 2.1, we have considered SSN from 1949 to 2019. The y-axis of the plot is the daily sunspot number, and the x-axis is the time. We can see from the graph that the time interval between two SSN peaks is around 11 years. In these 11 years, the SSN first take a peak and then minima or vice-versa. We have taken these data from SILSO. ¹
- **10.7 cm Radio Flux (F10.7 cm):** The F10.7 cm is actually solar radio flux density at 10.7 cm wavelength. This radio flux comes from the upper chromosphere and the low corona. As the emissions from the sun are highly vulnerable to the circumstances in the upper chromosphere and the low corona, we can also use the 10.7 cm flux number to track the solar activity. From figure 2.2, it is understood that F10.7 cm can also be used for monitoring the solar activity as the radio flux follows the 11-year solar cycle well.

¹Source: WDC-SILSO, Royal Observatory of Belgium, Brussels

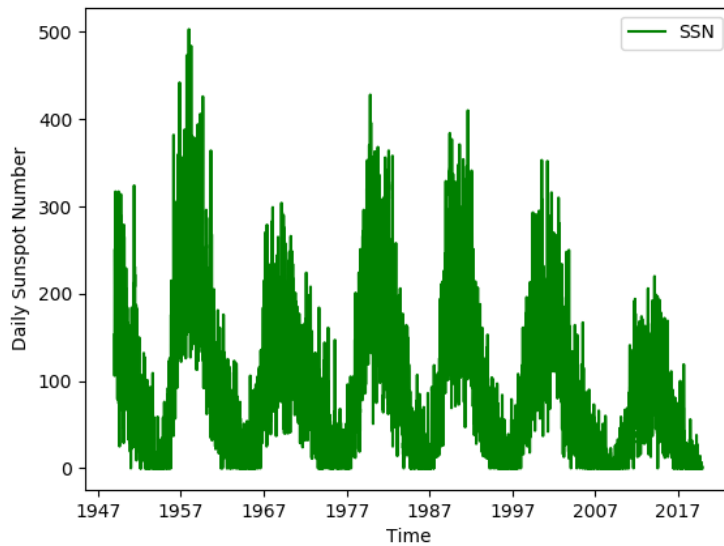


Figure 2.1: In the plot it is clearly visible that the sunspot numbers go from maxima to minima around 11 years. So looking at the time series, the information of when the sun is active or quiet can be known.

Hence, both sunspot number and solar radio flux at 10.7 cm can be used as excellent indicators of solar activity. In this work, the Penticton Solar Radio Flux at 10.7 cm dataset² has been used. At the first stage of this data tool, the code called Flux-Sunspot-Plotter was made. The schematic description in Fig. 2.3 tells what the code will ask from the user one the user runs it. First the user will be asked to give a date-time range and then the user will be given the option of downloading the database afresh or work with the existing archives which are already present in the folder. Based on these two processes, it will make three plots :

- Time series plot of daily sunspot number (SSN) and F10.7 cm
- Scatter plot of F10.7 cm flux vs SSN
- Histogram of slope values in the sunspot number and radio flux plane

²http://lasp.colorado.edu/lisird/data/penticton_radio_flux/

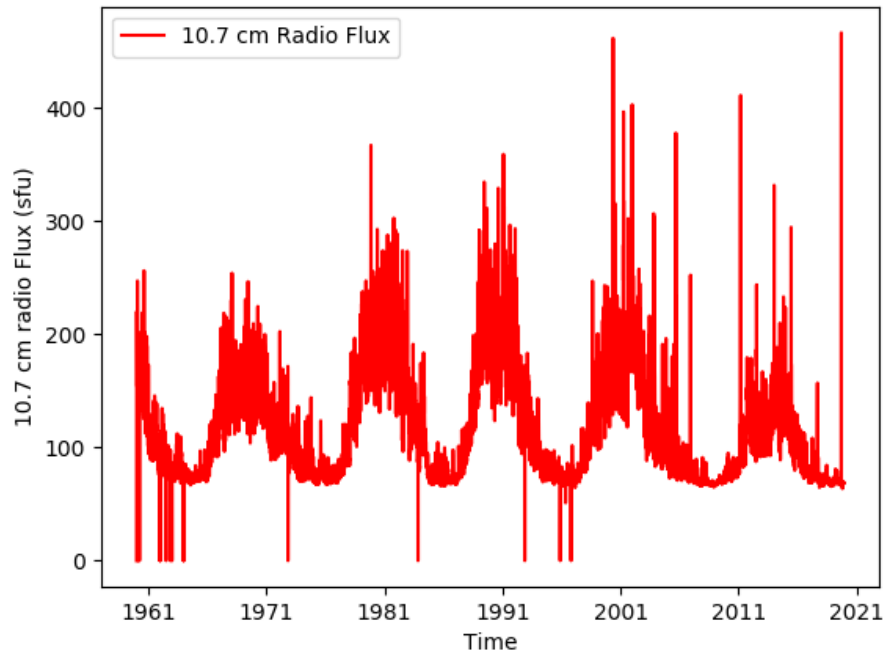


Figure 2.2: In the plot it is clearly visible that the daily solar flux go from maxima to minima in around 11 years. So looking at the time series, the information of when the sun is active or quiet can be known. The flux numbers are given in solar flux units (s.f.u' 1 s.f.u. = 10^4 Jy)

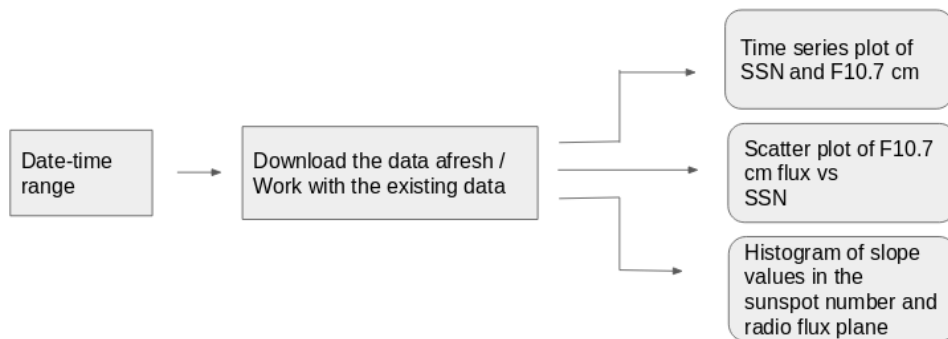


Figure 2.3: A Schematic description of the code

In the time series plot (Fig. 2.4), daily sunspot numbers and the 10.7 cm radio flux have been used as a proxy to tell us the state of the solar activity. Based on that information, the user can decide the range of interest.

We also wanted to check the linear correspondence between the daily sunspot number and the solar 10.7 cm radio flux. Therefore, in Fig.2.5, we have fitted a linear regression model

to the flux number and the sunspot number by assuming the sunspot number to be the dependent variable (y) and the radio flux (X) to be the independent variable. We thus obtained a 2-D plane of sunspot number and radio flux values, where every point represents the respective observations on a particular date. Then we calculated the slope of every point in our 2-D plane as we got the intercept value from the linear regression. After calculating the standard error of these slope values, we computed 1-sigma limits using the standard error of the array of the slope values. All the points in this plane are observed to be within a 3-sigma limit. We found out the correlation coefficient for the daily sunspot numbers and the F10.7 cm to be 0.87. We also plotted a histogram of the slope value of these points. Fig. 2.6 shows the spread of the slope values around the value predicted by our model.

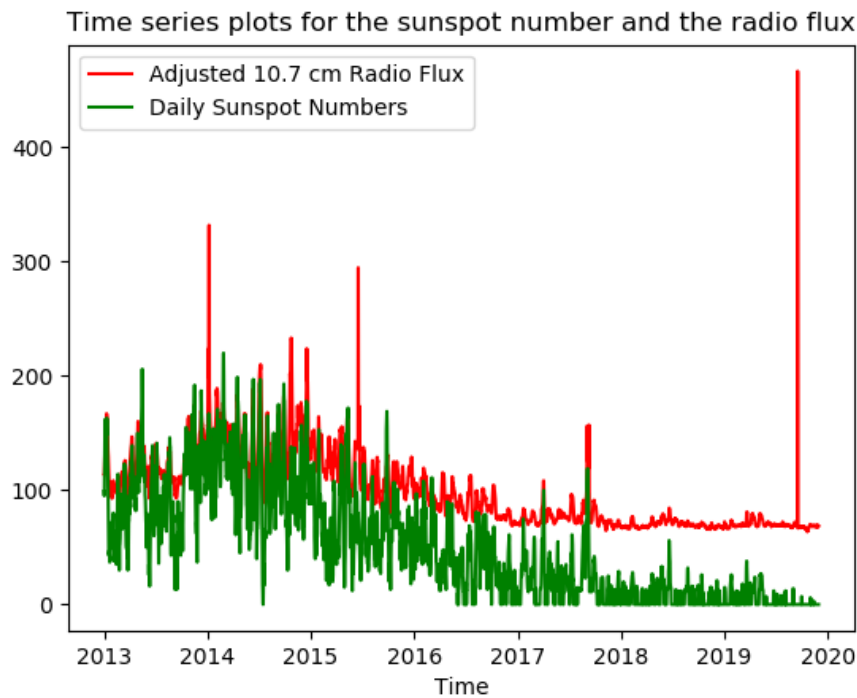


Figure 2.4: The time series of daily sunspot numbers (green) and F10.7 cm (red) can provide the user the state of the solar activity as both daily sunspot number and radio flux follow the 11 years solar cycle quite well. The observed flux numbers get affected by the distance between the Sun and the Earth. So to describe the Sun's behaviour, the standard distance of 1 A.U is considered and these flux numbers are called the adjusted 10.7 cm radio flux.

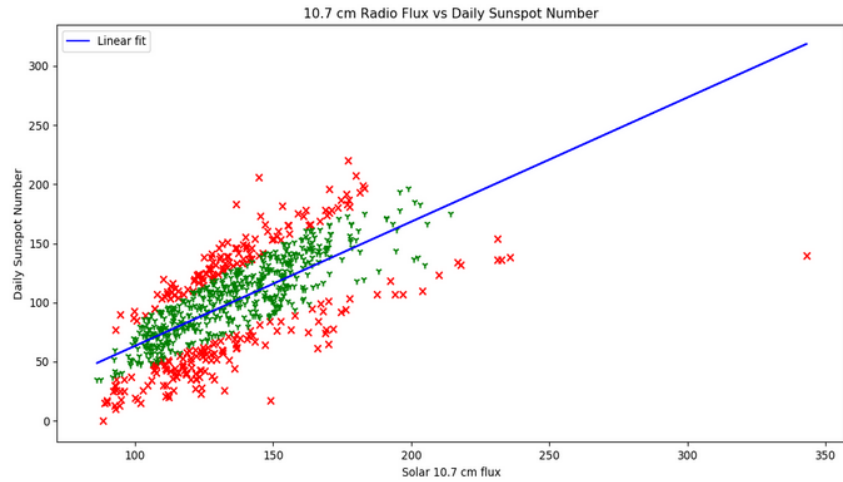


Figure 2.5: A scatter plot showing the linear regression analysis of Solar Flux F10.7 and daily Sunspot Numbers. The solid line represents the linear fit for flux F 10.7 and daily Sunspot Numbers. Here the green points correspond to the points within the 1-sigma limit.

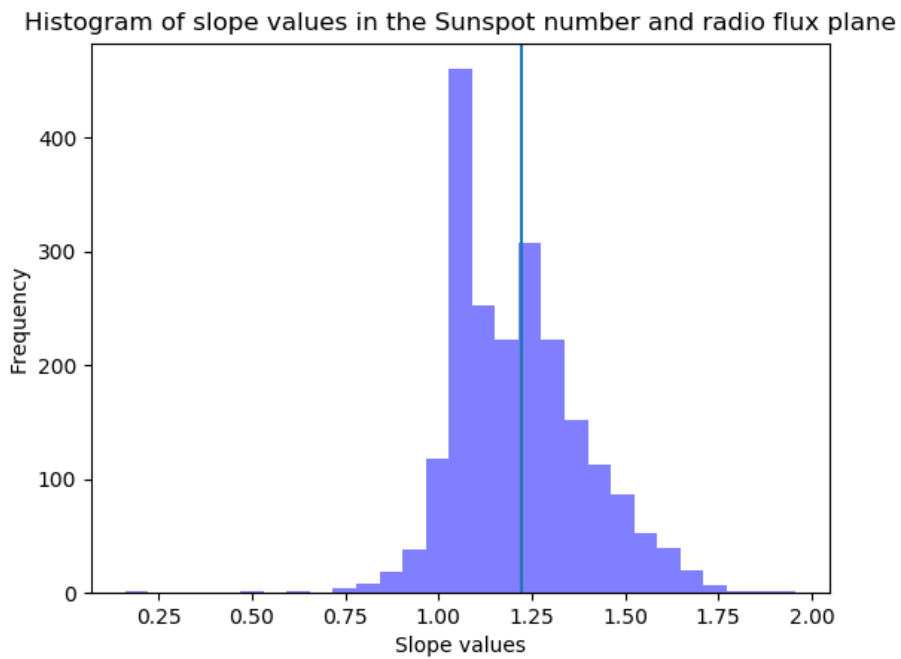


Figure 2.6: This histogram shows the spread of the slope values around the value predicted by our model.

2.2 Coronal Mass Ejection(CME) & Solar Flares

- **Coronal Mass Ejection (CME):** CME is the sudden release of the plasma and the magnetic field from the corona, propagating outward into the interplanetary space.
- **Solar Flares:** A solar flare can be seen as a sudden, fast variation in brightness on the Sun, near the sunspots. This sudden release of the energy becomes noticeable in the electromagnetic spectrum from the radio waves to the gamma rays. The flares can be classified as A, B, C, M or X according to their X-ray brightness in 1-8 Angstrom band.

These CMEs and flares are caused by magnetic reconnection process. These events can also give rise to geomagnetic storms, radio blackouts and many other catastrophic events. Therefore, it is essential to study these events. Keeping this in mind, we have chosen CMEs and flares as our next parameters to narrow down the time frame further. After running the script, the user will be asked to specify a range of interest based on the plots generated by the previous script. The script will download the respective data from the XRT flare catalogue³ and the SOHO LASCO CME catalog⁴. The full catalogues are downloaded and saved after which the DataFrames are sliced to the range of interest of the user. It will also ask if the user wishes to see just the total count of events for the given period or a full description of the events. For example, if the user gives the date as 11/06/2014 and time range from 01:00:00 UT to 09:10:00 UT, the script will provide the pieces of information of all the flares and CMEs which took place on that date and between the time range (Fig.2.10).

The script will then generate histogram of CME and flare counts for full data set(Fig. 8 and Fig. 9). The script will also open `solarmonitor.org`. As this website provides a lot of information such as:

- The list of all the events before and after the flare happened such as radio bursts.
- The X-ray, protons and electrons flux on the day the flare took place.
- Also gives an idea of the origin of the flare on the Sun.

³https://hinode.isee.nagoya-u.ac.jp/flare_catalogue/

⁴https://cdaw.gsfc.nasa.gov/CME_list/

Soft X-ray class	
Importance class	Peak flux in 1-8 Å w/m ²
A	10 ⁻⁸ to 10 ⁻⁷
B	10 ⁻⁷ to 10 ⁻⁶
C	10 ⁻⁶ to 10 ⁻⁵
M	10 ⁻⁵ to 10 ⁻⁴
X	>10 ⁻⁴

Figure 2.7: The figure gives the classification of the flares according to their peak flux in the wavelength range of 1-8 Angstrom band[2].

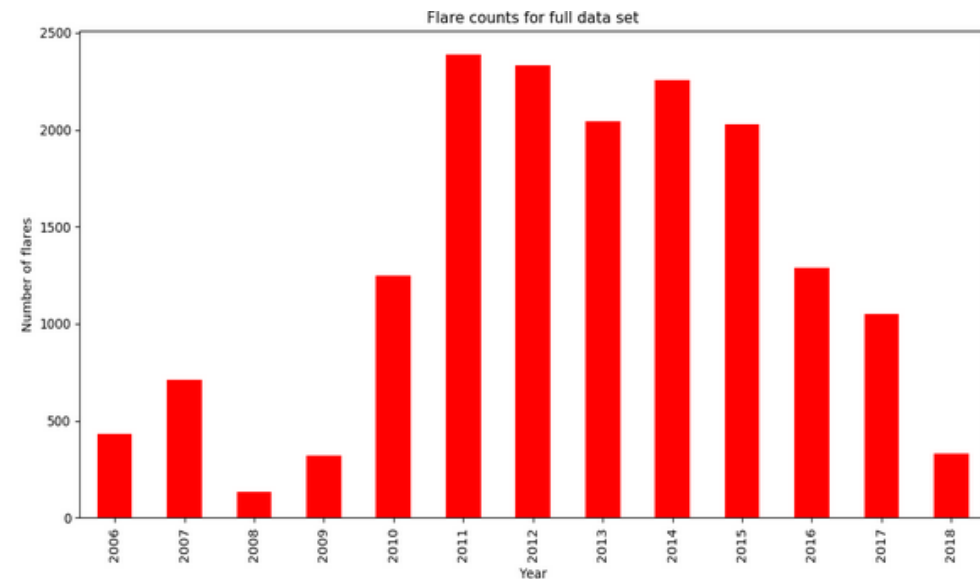


Figure 2.8: The figure gives the information about the total flare counts over the years.

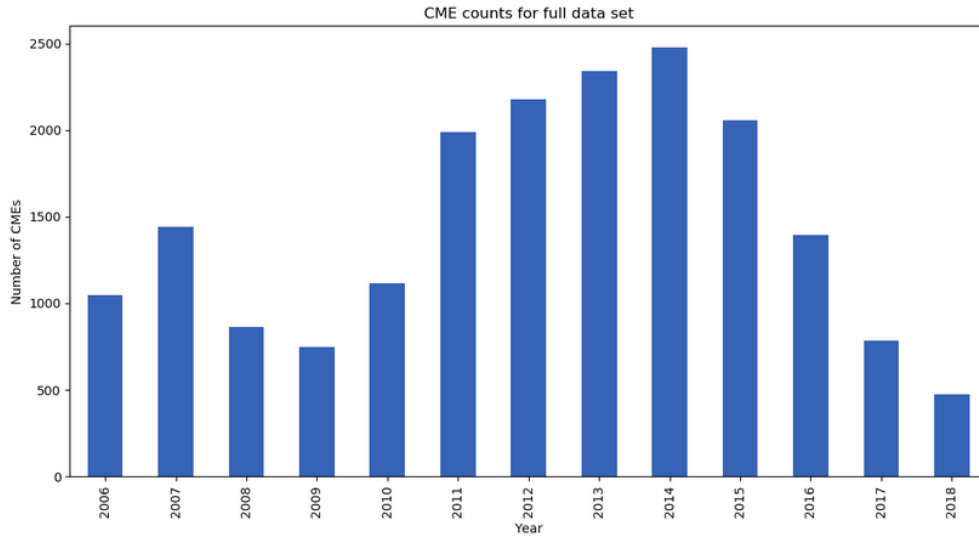


Figure 2.9: From the histogram plot The user gets to know about the total CME counts over the years.

Date	Time	Central	PA	Width	LinSpeed	2ndInitial	2ndFinal	2nd20R	Accel	Mass	Kinenergy
2014-06-11	00:12:05	106	30	966	849	1079	1214	32.0*	1.3e+14	6.1e+29	
2014-06-11	00:36:05	118	15	412	294	521	535	8.6*	-----	-----	
2014-06-11	00:48:06	62	44	343	272	402	482	6.7*	7.0e+14	4.1e+29	
2014-06-11	02:00:05	66	21	422	490	346	0	-12.7*	3.8e+14	3.3e+29	
2014-06-11	05:00:06	99	78	834	944	713	756	-13.8*	1.0e+15	3.6e+30	
2014-06-11	07:36:05	217	81	491	372	600	797	20.9*	5.8e+14	7.0e+29	
2014-06-11	08:24:05	97	103	773	852	695	705	-9.6	1.5e+15	4.5e+30	
2014-06-11	08:36:05	45	100	346	249	456	462	6.3*	1.6e+15	9.9e+29	

id	start	end	peak	loc1	class	X	Y
106540	2014-06-11 01:22:00	2014-06-11 01:30:00	2014-06-11 01:28:00	N17E30	C3.9	-449.0	270.0
106550	2014-06-11 02:56:00	2014-06-11 03:10:00	2014-06-11 03:02:00	N13W28	C2.3	447.0	206.0
106560	2014-06-11 04:39:00	2014-06-11 05:18:00	2014-06-11 04:44:00	S17E71	C5.0	-848.0	-282.0
106570	2014-06-11 05:30:00	2014-06-11 05:36:00	2014-06-11 05:34:00	S12W35	M1.8	533.0	-204.0
106580	2014-06-11 06:26:00	2014-06-11 06:37:00	2014-06-11 06:32:00	S13E69	C3.4	-840.0	-300.0
106590	2014-06-11 07:08:00	2014-06-11 07:20:00	2014-06-11 07:12:00	S13W35	C2.8	555.0	-207.0
106600	2014-06-11 08:00:00	2014-06-11 09:52:00	2014-06-11 08:05:00	S14E68	M3.0	-836.0	-305.0
106610	2014-06-11 08:59:00	2014-06-11 09:10:00	2014-06-11 09:06:00	S18E65	X1.0	-825.0	-300.0

Figure 2.10: After running the code, the script will produce two catalogues. The topmost catalog will provide information about all the CMEs which took place on 2014/06/11 during the time range from 01:00:00 UT to 09:10:00 UT. The 3rd column denotes the central position angle (PA). Here LinSpeed refers to the linear speed which was evaluated by fitting a straight line to the height time measurement. The 2ndInitial and 2ndFinal were gotten by fitting a second order polynomial to the height time measurement and evaluated at the time of first and final possible measurement. The bottom catalog gives all the informations (start, end and peak time, location, X and Y coordinates) about the flares which took place on the above mentioned date and time.

2.3 Geomagnetic Indices

The previous parameters provide the information on the Sun. To give the user an idea about how the various solar activities effect the near-Earth atmosphere, we have considered the various geomagnetic indices (Kp, ap and Ap).

- Kp index: It describes the variation in the geomagnetic field.
- ap index: it is the linear scale converted from each Kp value.

<i>Kp</i>	0o	0+	1-	1o	1+	2-	2o	2+	3-	3o	3+	4-	4o	4+
<i>ap</i>	0	2	3	4	5	6	7	9	12	15	18	22	27	32
<i>Kp</i>	5-	5o	5+	6-	6o	6+	7-	7o	7+	8-	8o	8+	9-	9o
<i>ap</i>	39	48	56	67	80	94	111	132	154	179	207	236	300	400

- Ap index: Average of ap values for each day.

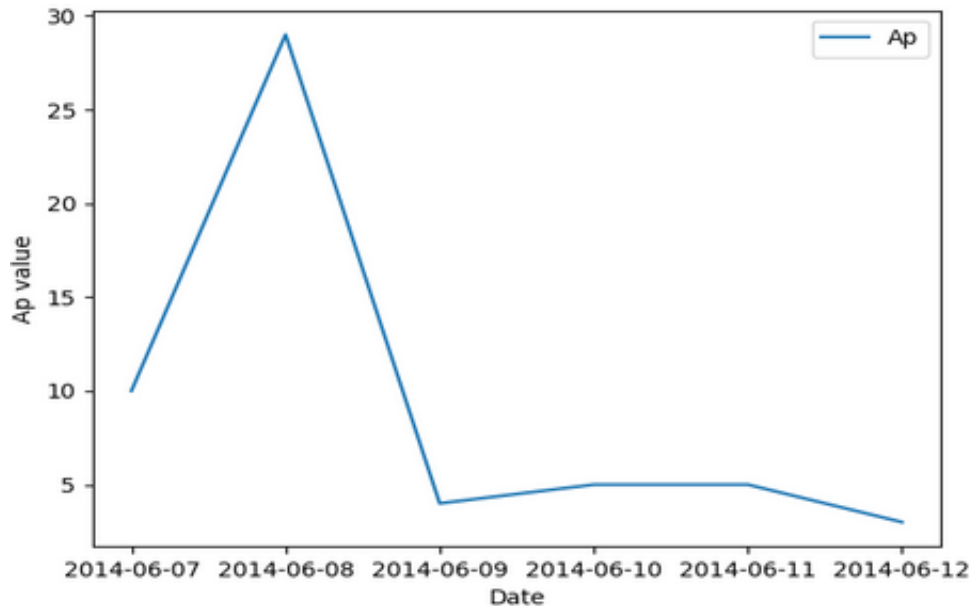


Figure 2.11: In the figure, the Ap values are plotted for the date range from 2014-06-07 to 2014-06-12.

We have written a script which accepts a range of dates based on the outputs of the previous two scripts and then downloads the geomagnetic index (Kp) data, creates a

DataFrame and converts the downloaded Kp values to ap values ⁵. It then calculates the average value of the ap index and plots it for the reduced time range of the user's interest to check for effects of solar activity on the near-earth environment in that period (Fig.2.11). The DataFrame is then sliced to the user's range of interest and both the full DataFrame and the reduced DataFrame are saved to text files as well.

2.4 Probing the MWA data

After choosing the date-time frame of our interest, it is very important to check the MWA database if we have the observations for that frame. This script downloads the observation IDs of MWA observations ⁶ for a date-time range specified by the user and converts them from GPS time to UTC factoring in leap seconds. The UTC format data frame and the GPS format data frames are both saved as text files once the execution of the script is complete. After downloading the data, it will give total number of observations for range of interest and also a list of observations with date and time. Here we have also taken into account of the data quality. There are various data quality flags(digits from 1 to 6), where 1 good, 2 some issues, 3 unusable, 4 deleted, 5 marked for deletion, 6 processed. We are only considering 1 and 2. The reason behind choosing the second data quality was that there can also be data for which only the only half freq channels got recorded. The script will also generate a histogram of the number of observations for the full data set (Fig.2.12).

⁵<https://www.gfz-potsdam.de/en/kp-index/>

⁶<https://wiki.mwatelescope.org/display/MP/Web+Services>

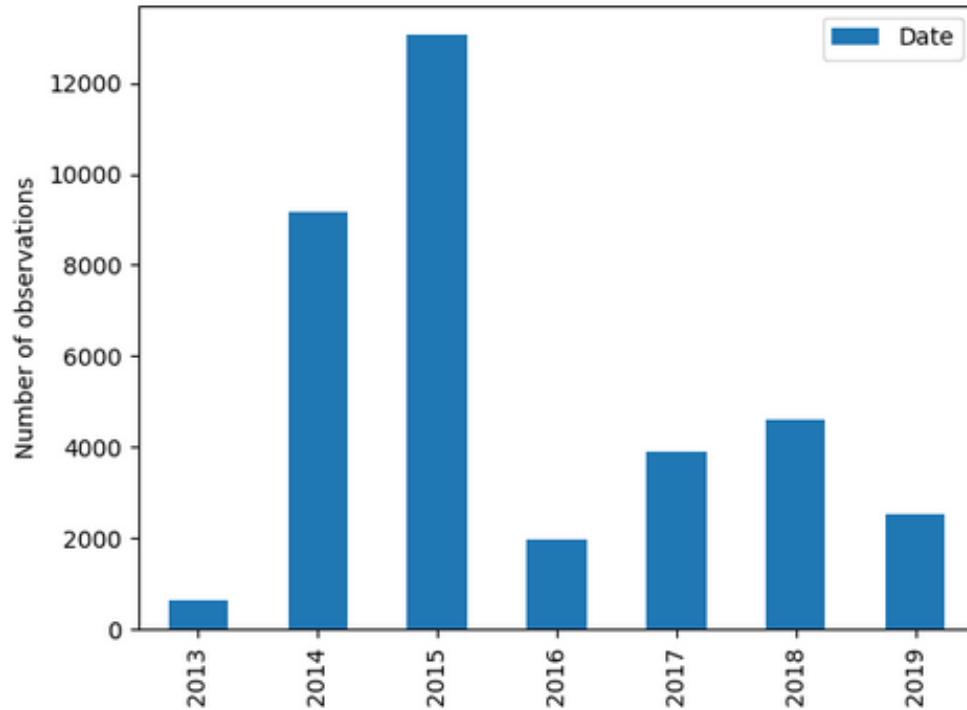


Figure 2.12: The figure gives an idea about how many MWA solar observations are there over the years .

Till this point, the algorithm was built in such a way that it will help the user to choose the MWA data based on the previous mentioned parameters. But what if the user needs MWA data, for example,

- When the sunspot number is between 50 to 70.
- When there is CME.
- When there are X or M class flares.

Keeping this in mind, we have written a script which asks the user to specify an operation of their choice. The user can query based on Sunspot number, Radio Flux, Flares, CMEs and Class of the flare. For example, if a user chooses M class of flare, then the script will ask for a date-time range. Based on that range, it will produce the list of M class flares and the list of MWA observations. Then the user will be asked for the date and the time for the flare they have in mind. The program also opens the SOHO LASCO CME catalogue for

the month in which the chosen flare has occurred and opens the `solarmonitor.org` webpage for the day on which the flare event has taken place. This webpage links to a list generated by the Space Weather Prediction Center (SWPC) that the user is encouraged to consult as well.

For my thesis work, I have chosen a type II radio burst associated with M5.1 class flare identified using the query data tool to analyze.

Chapter 3

Imaging Process

The type II radio burst started around 02:45:00 UT and ended at 02:55:00 UT on 28/09/2014. The reason why we are saying that it is associated with the flare is because from SWPC event list it has been observed that the time range of both of these events overlaps and their origin is also same. We have chosen 4 MWA data set to see what happened before the burst, during the burst and after the burst. Each of these data set is 4 min long and only half of the frequency channels are there in the data set. These frequency channels are 62-63, 69-70, 76-77, 84-85, 93-94, 103-104. Each of these groups of channels spans ~ 2.56 MHz. Before we start analyzing the data, we need to remove the instrument artifacts from the data and calibrate them. For that, we passed the data through AIRCARS, an robust and effective imaging pipeline developed specifically for the MWA data, followed by the flux calibration process. The description of both these processes are given in section 3.1 and 3.2 respectively.

3.1 Automated Imaging Routine for Compact Arrays for the Radio Sun (AIRCARS)

In radio astrophysics, it is very important to remove the instrumental and propagation effect. from the data set before we start analyzing the data. Because of the enormous data volume of MWA, manual calibration and imaging is not possible. The problem has been

solved by the recent development of AIRCARS. It can produce images of dynamic range (DR) as high as $\sim 100,000$. DR is defined as the ratio of maximum intensity to the rms of the image far away from the sun. The DR indicates how well we can identify the low intensity features in the presence of strong sources in the image. So it is very important to have images with high DR, which AIRCARS is able to provide. The algorithm has two steps. The first step is to take into account the decorrelation due to instrumentation and the second step involves self calibration. Both of these processes are described respectively in the following sections.

3.1.1 Correction of Visibility Due To Decorrelation

From section 1.2.2, it is clear that averaging over one spectral channel leads to the attenuation of fringe amplitude and to eliminate that we need to do the delay tracking. But the MWA correlator does not have a delay model. It just cross correlates the signal coming from two antennas, which tells us that we have to calculate this amplitude loss so that we can get corrected visibility. Then the reduced fringe amplitude, a_{cor} is given by

$$a_{cor} = \frac{1}{\Delta\nu} \int_{-\Delta\nu/2}^{+\Delta\nu/2} \exp^{i2\pi\nu\tau} d\nu = \text{sinc}(\tau\Delta\nu) \quad (3.1)$$

Here $\tau = \tau_{1,2} + \tau_g$, where τ_g is the geometric delay, $\Delta\nu = 40\text{kHz}$ and $\tau_{1,2} = \tau_2 - \tau_1$ is the delay due to varying cable lengths of antennas 1 and 2. Hence, the corrected visibility V_{cor} will be

$$V_{cor} = \frac{V_{obs}}{a_{cor}} \quad (3.2)$$

This correction can only be done for one direction. As a_{cor} only depends on the cable lengths and where the source is, we should see a similar level of improvement irrespective of whatever is happening in the sun.

3.1.2 Calibration of Antenna Complex Gains

We do calibration to correct propagation effects and instrumental effects from the true sky signal. The propagation effects can include phase fluctuations due to water vapor in the atmosphere or ionospheric effects especially in the low frequency case etc. As the

propagation effects are indistinguishable from the instrumental effects, we can write $g_i = g_{i,inst} \times g_{i,prop}$ where

$$g_i = a_i \exp(i\phi_i) \quad (3.3)$$

In Eq.3.3, a_i is the antenna gain and ϕ_i is the phase of signal coming from the i th antenna with respect to the the reference antenna (the antenna for which the phase is assumed to be zero). Then the calibration equation is

$$V_{ij} = G_{ij}(t)V_{ij}^{tr}(t) \quad (3.4)$$

where V_{ij} and $V_{ij}^{tr}(t)$ are the observed and true visibility for the ij th baseline respectively. $G_{ij}(t)$ is the complex gain for the ij th baseline.

$$G_{ij}(t) = a_i a_j \exp[i(\phi_i - \phi_j)] \quad (3.5)$$

Here a_i and a_j are the amplitude part of the gain terms and ϕ_i and ϕ_j the phase part. Ideally, $(\phi_i - \phi_j)$ should be zero if there is no atmospheric effect and if all antenna electronics are identical. We can get the antenna gains by using signal coming from one of the calibrator sources. Calibrator sources are sources about which we know everything like position, flux density, structure etc. But then these calculated g_i s will be different from those derived from the target source, as there will be some time and direction difference between the calibrator source and the target source. We can solve this issue by doing self-calibration where both the g_i and the sky model are free parameters. Then we iteratively minimize the difference between the observed data and the true sky model, which implies the convergence of this method depends on the quality of the true sky model.

3.1.3 Improving the Image Quality

Deconvolution: It is already known that

$$I(x, y) = \int \int V(u, v) \exp 2\pi i(ux + vy) du dv \quad (3.6)$$

But we do not get the correct visibility as the whole u - v plane can not be filled with the antennas with all possible baseline and directions. Hence, instead of getting the correct

visibility we get V^{Ob}

$$V^{Ob} = V(u, v) \cdot S(u, v) \quad (3.7)$$

Here $S(u, v)$ is the sampling function the value of which is 1 where u - v sampling is done and zero otherwise. Fourier transform of Eq. 3.7 gives us

$$F^{-1}[V^{Ob}] = F^{-1}[V(u, v)] * F^{-1}[S(u, v)]$$

$$I^D(x, y) = F^{-1}[V(u, v)] * F^{-1}[S(u, v)] \quad (3.8)$$

$$I^D(x, y) = I(x, y) * I^{PSF}(x, y) \quad (3.9)$$

Here $I^{PSF}(x, y)$ is the dirty beam or the point spread function (PSF). The shape of the dirty beam is determined by how filled the u - v plane is. The dirty image is the convolution of the dirty beam and the true image. As we are interested in the true image, we need an algorithm which will remove the side lobes of this PSF from all regions of the true sky image.

One can say as the location of the antennas are known, we can get $V(u, v)$ by dividing $I^D(x, y)$ by $S(u, v)$. But then $S(u, v)$ also contains zero leading to a divergence problem. Not only that, assuming zero in the unmeasurable part of the data is not correct because that will mean there is no contribution coming from that part of the uv plane. We also can not just assume random numbers as it will lead to multiple images accordant with the data. Hence we need an algorithm that will give us reasonable visibility in the unmeasurable part of the image without adding many random details.

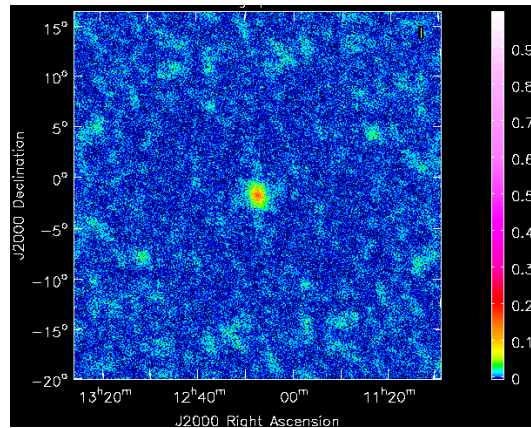


Figure 3.1: The figure shows the point spread function of MWA.

CLEAN: Let's consider that the sky consists of point sources, and each of these will be present as a copy of the PSF in the dirty image. The intense features in the map do not rigorously correspond to the positions and strength of the sources because each maximum gets affected by the side lobes of the PSF. The CLEAN algorithm first starts with detecting the brightest point in the image. Because even though it is getting affected by the side lobes, we can assume that at that point, the source is sitting. Then, the dirty beam will be shifted to that point, and a copy of the PSF, scaled to a fraction of the strength of the detected source, will be subtracted from that point. The fraction is called the loop gain. If the value of the loop gain is high, then there is a chance that we will not be able to detect the weak features, and if the value is too small, then the whole process will take too much time, making it computationally heavy. So choosing the right value for the loop gain totally depends on what kind of sources are there in the image. After the subtraction, the position and the flux will be noted down. This whole process will be done again and again till the point there will be nothing left, only the noise in the map, which is called the residual map. We call the collection of these point sources CLEAN components. One can say that these CLEAN components are the solution. But there is an issue of resolution. To reflect the resolution, the components are convolved with a Gaussian (known as the restoring/CLEAN beam). We keep the dimension of the CLEAN beam same as the main lobe of the dirty beam. Because higher the $\frac{b}{\lambda}$, the resolution also increases. And finally we get the intensity map convolved with the CLEAN map.

Self-calibration In the calibration process, we know the sky model very well and the gains are determined from the calibrator sources. In the self-calibration process, the antenna gains are obtained by minimizing ϕ

$$\phi = \sum_{ij} |V_{ij} - g_i g_j^* V_{ij}^M| \quad (3.10)$$

FI^M is the Fourier transform of the model sky image and is used to compute $V_{i,j}^M$. In the case where the actual sky model is unknown, we treat the antenna gains and the sky model as free parameters. We use least squares solution to get the gains. The reason behind its success is that the problem is over determined. In the array, there are n antennas and if one of the antennas is taken as the reference antenna, then there are total $2(n-1)$ error parameters and the number of equations is $n(n-1)/2$. The process of minimizing ϕ is an

iterative process. The steps are

1. Get the observed visibility and do the Fourier transformation to get the sky image.
2. CLEAN the image to produce a new model.
3. Check if the process has converged or the improvement of the image quality has declined. If not, then go to the next step.
4. Fourier transforming the new model to give the new set of visibilities $V_{ij}^{M'}$, and use that set of visibilities to get the new gains.

The whole process should be repeated until it converges and we get the g_i s close to 1.

3.1.4 Advantage of having dense array cores

From the dense core, we pick an antenna as a reference antenna and get the antenna gains for other antennas with respect to that antenna. For the core antennas, the $g_{i,prop}$ will be very close to one. For the MWA, we can only observe calibrator sources when the sun is below the horizon and hence the time interval of the estimated $g_{i,inst}$ from the calibrator observations and the actual solar observation is huge. For the antennas very far from the reference antenna, $g_{i,prop}$ will diverge from one. The g_i s we get from the core antennas give us a very good initial guess of a low resolution sky model. All the antennas are always used to get the antenna gains. The way we do is an iterative process. In each iteration, antennas are added at increasing separation from the reference antenna until the entire array is used for making the source model. In Fig.3.2, it is shown that how the MWA antennas are added. In each iteration, we will get a new source model after correcting the data utilizing the g_i from the previous iteration(s). After adding all the antennas, we are at a point where we can start the usual self-calibration cycle. The process converges when the improvement of the dynamic image range is lesser than the user-specified amount in the present iteration, and we say the process has diverged if a large steady decrease in the DR of the images is found. Self-calibration is also stopped if the number of iteration steps is more than the maximum number of iterations is specified by the user. In either of these cases, we stop the self-calibration. From Fig. 3.3, it is evident that the image quality improves as the number of the self-calibration iteration increases. In such a case, the self-calibration is started over again using the original approach of iterative addition of antennas. If, in this case, also the convergence does not happen, we skip the self-calibration for the current time slice and keep it for future examination.

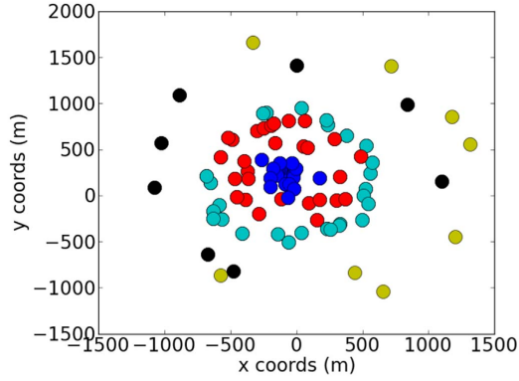


Figure 3.2: The figure shows how the antennas are added for MWA. In first step, antennas marked with blue are added. Then in the following steps, antennas marked with red, cyan, black and yellow are added.

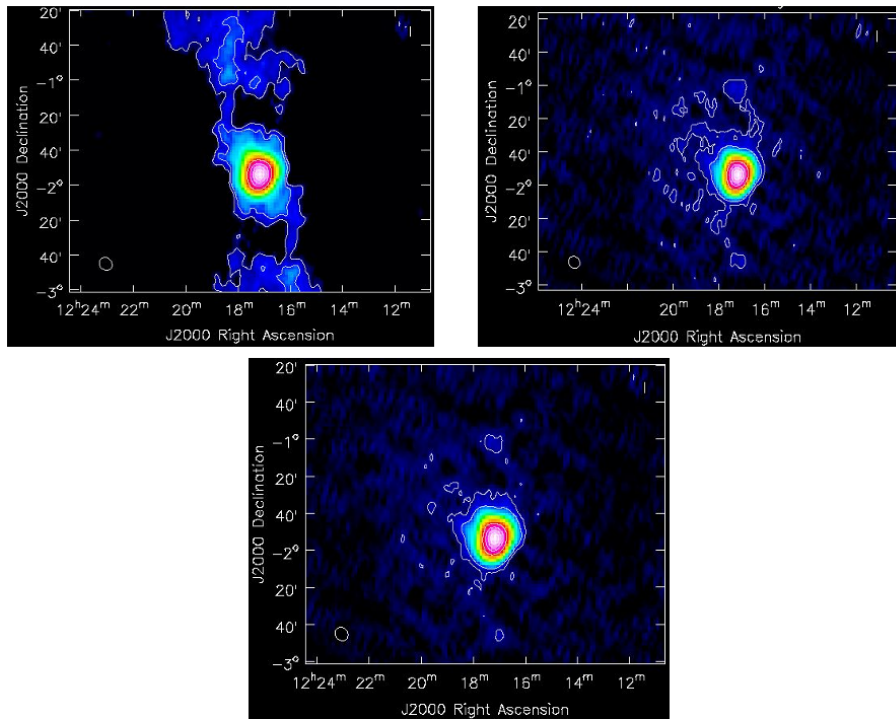


Figure 3.3: The top-right, top-left and bottom images are acquired after 25, 40 and 91 self-calibration iteration respectively. The contours are labeled at 0.0015, 0.05, 0.2, 0.6, 0.8 times the peak intensity in the image. Clearly as the iteration number increases, the image quality also improves.

3.1.5 The Robustness of AIRCARS

Using AIRCARS, we can obtain images of high fidelity and DR. The reasons behind getting such images are the following factors: 1. High flux density from the Sun gives high SNR signal, which allows us to calibrate the data to very high accuracy and hence make high DR images. High flux density from the Sun gives high SNR signal. So we can detect small changes in the emission morphology of the Sun.

2. The large number of antennas of the MWA array provides some advantages. The issue of solving the g_i becomes significantly over-constrained with a large number of antennas. The arrangement of antennas is such that it produces PSF with low side lobes, advantageous for doing automated self-calibration and making the problem of deconvolution easier.

3. The dense core of the MWA allows the software to achieve the robust gain calibration while using the almost unresolved sun. Also, the inclusion of antennas in successive iterative steps adds a small number of new degrees of freedom at a moderate rate where we have a good guess about previous g_i s and the source model at low resolution.

3.2 Flux Calibration

As the Sun is much stronger than the typical radio sources studied by the modern sensitive radio interferometers, it becomes necessary to attenuate the strength of the solar signal so that it lies within the linear range of the downstream signal chain. This allows one to make reliable quantitative measurements. The typical calibrator sources used in radio astronomy are however much weaker and not observed using additional attenuation used for solar observations. This has the consequence that the solar observations cannot be calibrated using the usual radio astronomy procedures. An independent flux calibration technique was hence developed for calibrating solar MWA data Oberoi2017 (The reference is available at - <https://ui.adsabs.harvard.edu/abs/2017SoPh..292...75O/abstract>).

For our observations we make use of wide field-of-view of the MWA, the high DR imaging capability of AIRCARS, and the fortuitous presence of, VIRGO-A, a strong and very well studied radio source, in the field-of-view, and use it as a calibrator source (Fig 3.4). We used NASA/IPAC Extragalactic Database (NED) to obtain the expected flux densities of VIRGO A, based on spectral index determined using observations over a large range of

frequencies overlapping with our observations. Then we accounted for the attenuation factor because of the primary beam of the antenna. Once all these values were determined, we were able to get the scaling factor by which the flux density of the VIRGO A in the images has been reduced. Then we multiplied these images with the scaling factor. All these processes are described in the following sections:

3.2.1 Cleaning The Region around the VIRGO A

When we pass the data through AIRCARS, the default settings of the CLEAN algorithm only work with the inner quarter of the full image. As we can see from the Fig.3.4, that VIRGO A lies outside this region, towards the top of the image. In order to include this region of the map, a circular mask was placed around VIRGO A (Fig 3.4), as mentioned the region in the parameter called maskfile in AIRCARS. It is obvious from the right image of Fig. 3.5 that the process has managed to clean the side lobes around the VIRGO A. This cleaning is necessary to get the correct scaling factor for the Sun.

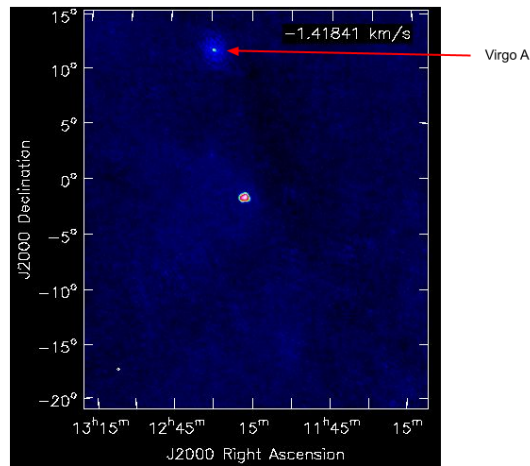


Figure 3.4: In the image the VIRGO A has been marked by the red arrow. The bright compact region around the centre of the image is an emission region on the Sun. While the emission around the Sun has been CLEANed, that around VIRGO A has not.

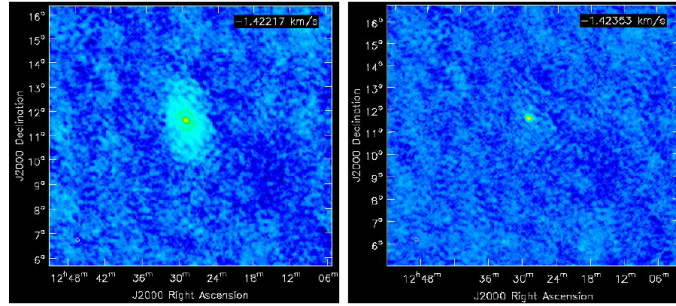


Figure 3.5: The two panels show the region around VIRGO A, before and after CLEANing. In the left image, we can see some extended structures around the VIRGO A, which is not there in the right image. This tells us that the quality of the image has improved around the VIRGO A after we have done the cleaning around the source.

3.2.2 Determining The Actual Flux Density of VIRGO A

We used NASA/IPAC Extragalactic Database (NED) to get the VIRGO A flux for different frequencies. Our range of interest for frequency falls between 79.36 and 133.12 MHz. But NED did not have enough data for this range. So we took flux values and the errors for frequency range from 10^7 to 1.41×10^9 Hz from NED and logarithmically scaled both axes flux density and frequency. In the Fig. 3.6, linear regression model has been fitted over the values with error bars.

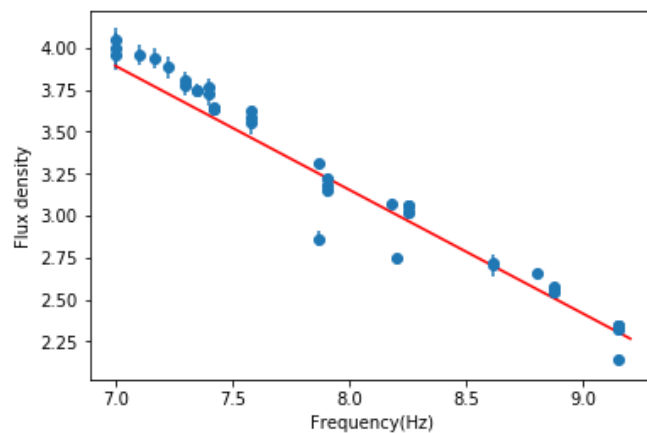


Figure 3.6: A plot showing the linear regression analysis of $\log(\text{flux density})$ and $\log(\text{frequency})$. The solid line represents the linear fit for these values.

We assumed y and x to be $\log(\text{flux density})$ and $\log(\text{frequency})$ and the equation we got is

$$y = -0.7392x + 9.0683 \quad (3.11)$$

where the errors on the slope and intercept are 0.0023 and 0.1524 respectively.

3.2.3 Deriving The Primary Beam Pattern of MWA

When the monochromatic light passes through a single slit, we have a central maxima and many fainter maxima on both sides. Similarly an antenna's response to the radiation coming from the source is a function of the direction (Fig.3.7¹). We can call this response by $P(\theta)$. In Fig.3.7, at $\theta=0$, there is a central maxima which is called the main lobe and as θ increases, there are many smaller maxima called side lobes. At $\theta=0$, $P(0)=1$ but as the θ increases, $P(\theta)$ decreases. It means that if for some θ , $P(\theta) = 0.5$ and the actual flux density is S , then the flux density we will get is $0.5S$. So we need to divide the whole image by the primary beam pattern to correct the fluxes of the sources.

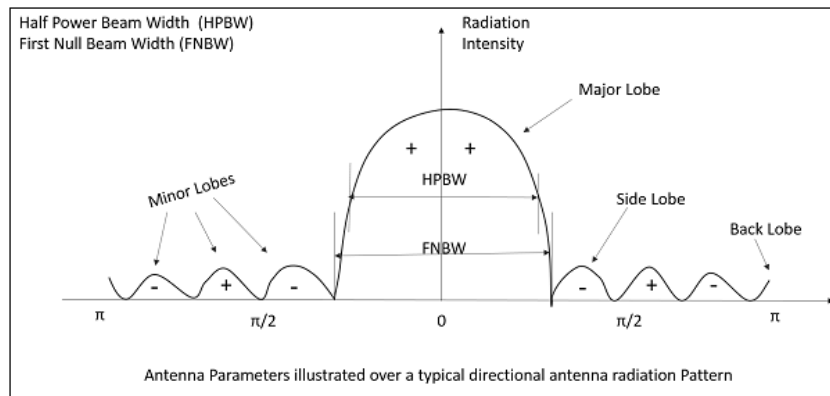


Figure 3.7: Power Pattern of an antenna¹

The Fig. 3.8 describes the main lobe of the MWA. In the image, we can clearly see the value of the attenuation factor goes from 1 to close to 0. We obtained Fig. 3.9 by dividing the image by the primary beam pattern of MWA. At the edges of Fig.3.8, the value become very small. Because of this, in Fig. 3.9, at the corners of the image, the noise increases.

¹https://www.tutorialspoint.com/antenna_theory/antenna_theory_beam_width.htm

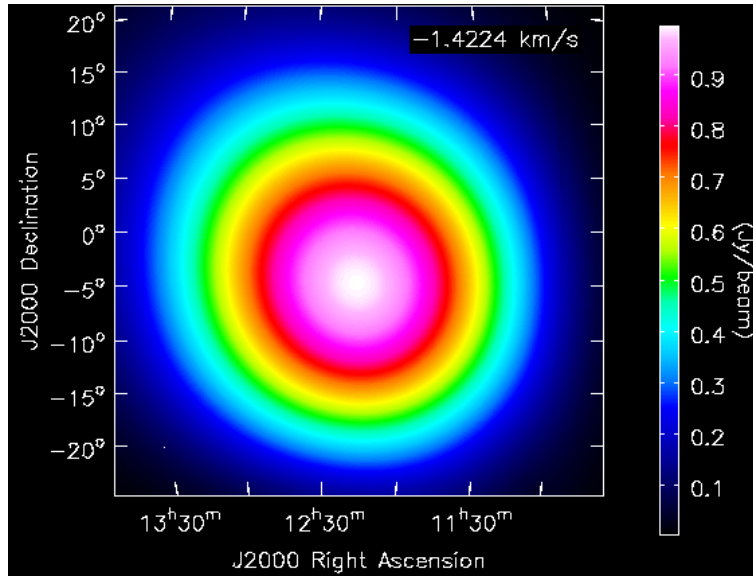


Figure 3.8: The primary beam pattern of MWA.

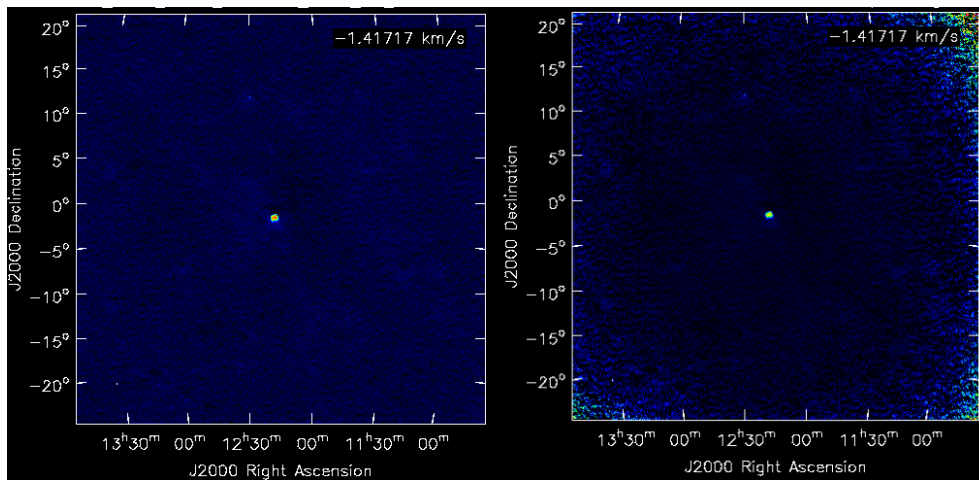


Figure 3.9: The right panel has been gotten by dividing the left image by the MWA primary beam pattern (Fig. 3.8). In the figure, we can see a circular dark region around the central bright region which is because at the centre of the image the number of the primary beam is close to 1. We can see the noise peaks at the corners of the right image due to division by the primary beam.

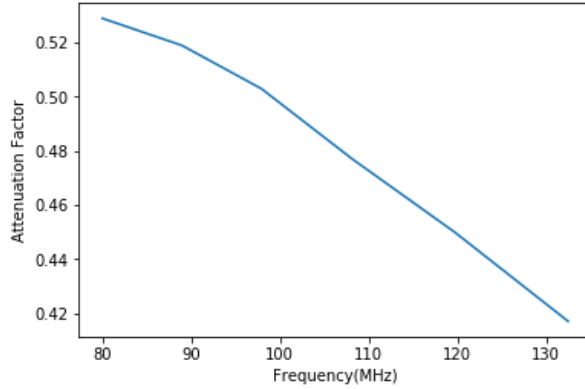


Figure 3.10: In the figure, it is apparent that as the frequency increases, the attenuation factor also falls down.

As the width of the main lobe is proportional to λ , the attenuation factor reduces with the increase of frequency, which is evident from Fig. 3.10. So to account for this, we had to get primary beam images for different spectral channels.

3.2.4 Calculating the Scale Factor

We used Eq.3.11 to derive the actual VIRGO A flux for different frequencies. Then, we got the scaling factors by dividing these actual flux values by the primary beam corrected fluxes of VIRGO A. In Fig. 3.11, we have plotted these multiplicative factors as a function of frequencies.

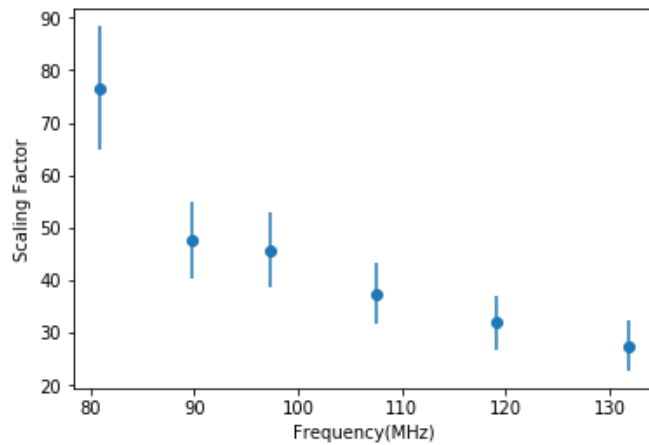


Figure 3.11: The plot shows how the scale factor changes with the frequencies.

In the end, we have used CASA task `immath` to multiply these scale factors with each of these frequency images. At this stage, we were done with our imaging processes and ready to start our analysis, which is described in the next chapter.

Chapter 4

Type II Radio Burst: Results and Discussion

Type II radio burst is often thought to be caused by the magnetohydrodynamics (MHD) shock accelerated electrons. These electrons produce Langmuir plasma waves through two stream instability, which in turn can give rise to radio emissions. The burst is seen to have appeared first at the high frequency, and then as the time progresses, it moves towards low frequency. This happens because the plasma frequency, f is proportional to $n^{1/2}$, where n is the electron density. So, as the burst which originates in the solar corona, moves radially outward from the sun, the electron density decreases. As a result, the burst moves to lower radio frequencies. Often, the burst is seen to have two emission lanes: harmonic and fundamental. But sometimes, both fundamental and harmonic type II emission can be organized into two sub-bands: higher (H) and lower(L) (Fig. 4.1). They are believed to be coming from downstream and upstream regions of the shockfront respectively..

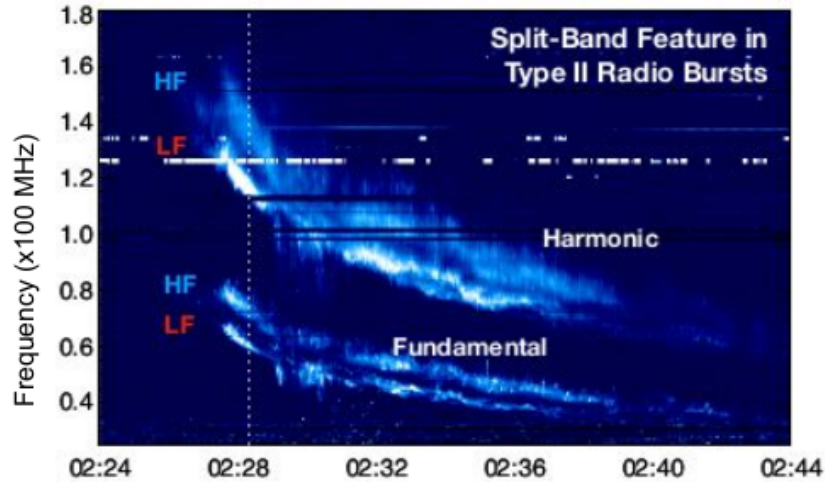


Figure 4.1: The figure is an example of an type II radio burst[3]. The high frequency (HF) and low frequency(LF) bands can be seen in both harmonic and fundamental emission.

4.1 Dynamic Spectrum

The type II burst seen in the Learmonth spectrograph (Fig. 4.2) started around 02:45:00 UT and ended at 02:55:00 UT. The portion of the type II burst, for which we have analysed the MWA data is marked in the purple box. The left panel of Fig. 4.3 is the dynamic spectrum observed in the MWA data. It is obvious from the dynamic spectrum that there are more finer structures in the harmonic band which MWA has been able to capture. Also, though the Learmonth spectrograph (Fig. 4.2) suggests that no fundamental emission would be seen in MWA data, however some fundamental emission can be seen at the bottom of the MWA dynamic spectrum. It is also apparent from the time series at the right panel, a cut across 79.98 MHz, where the first and second peaks correspond to fundamental and harmonic, respectively.

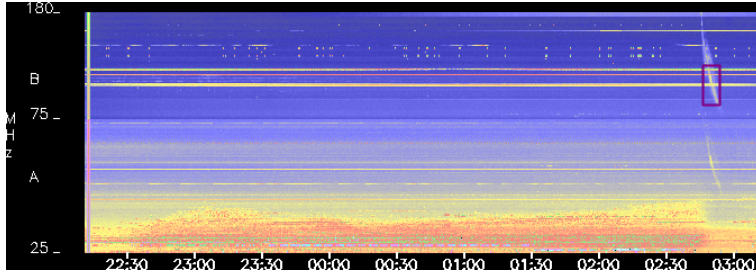


Figure 4.2: Dynamic spectrum of the type II burst in the Learmonth Spectrograph.

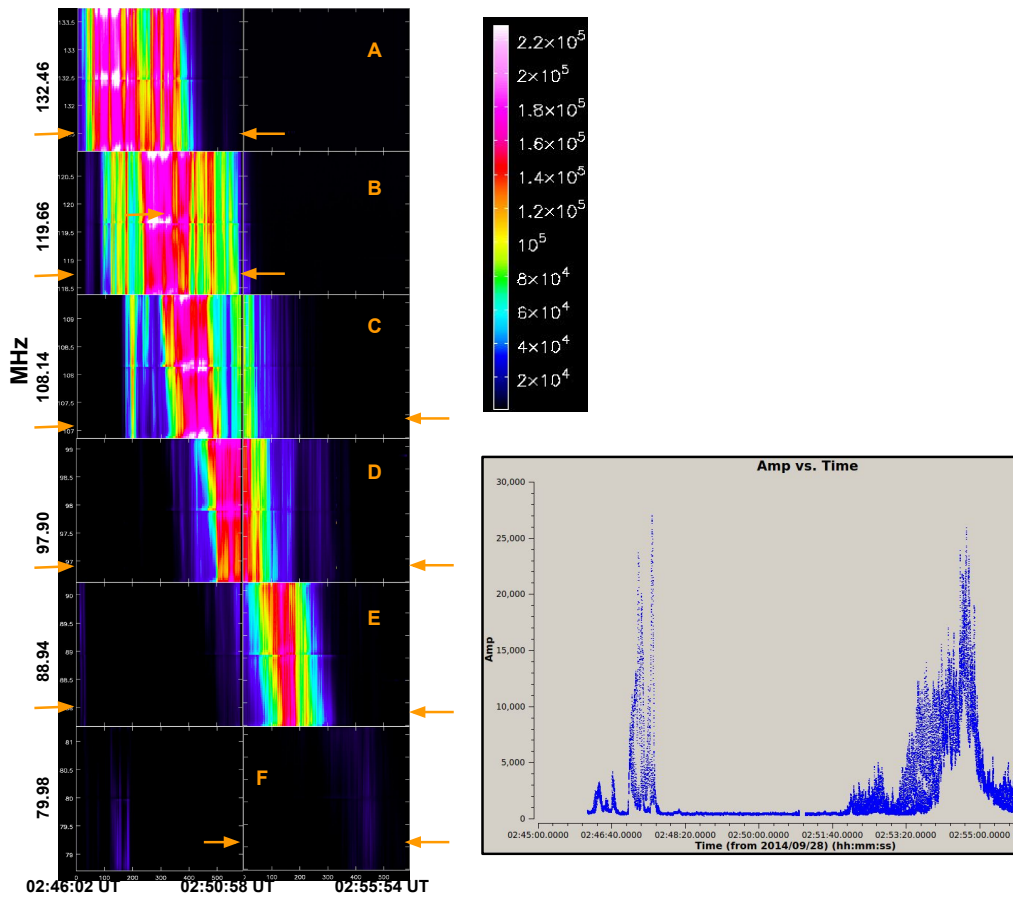


Figure 4.3: The left panel shows the dynamic spectrum as seen in the MWA picket fence data (zoom in from Fig. 4.2). It is evident that the MWA offers much cleaner data with higher sensitivity which reveal many details not seen in Fig. 4.2. The central frequency of each of the panels on the left side is mentioned, and each picket spans ~ 2.5 MHz. The observed emission corresponds primarily to the harmonic (H) band, with a tiny bit of fundamental (F) emission seen in the bottom left panel. The time series at the right panel is a cut across 79.98 MHz. The first peak corresponds to the F emission, and the second one to the H emission.

4.2 Example of Solar Images

In Fig. 4.4, we have shown some AIRCARS solar images. The frequency and time for each of these images are given in the top of the images.

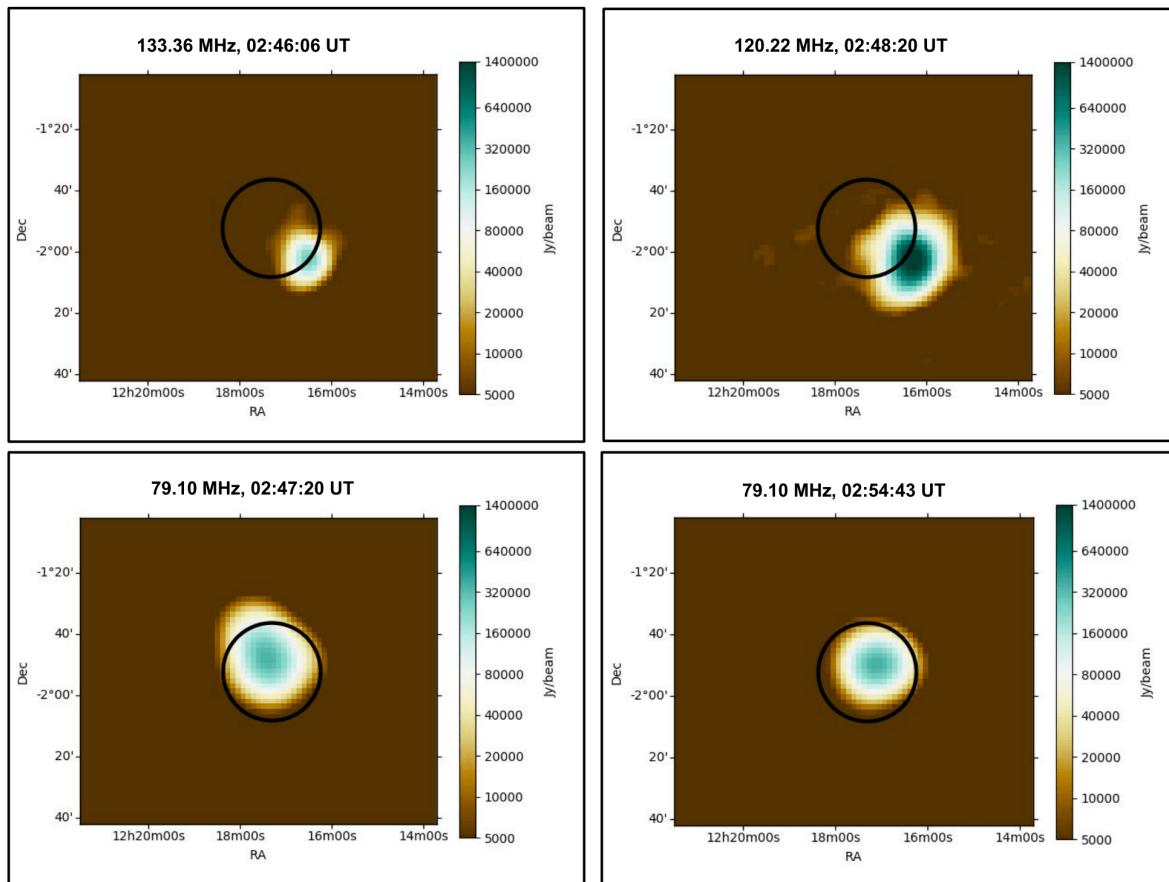


Figure 4.4: Some example MWA solar images. In all the images, the black circle represents the optical disc of the sun. The top left and right panels shows the weak and strong harmonic emission on the sun respectively. The bottom left panel represents the fundamental emission on the sun. The bottom right panel gives an idea about the morphology of the emission when the harmonic band was ending.

4.3 Analysis

We have already mentioned that sometimes both harmonic and fundamental emission of type II burst is seen to be organised in two bands of emission. But in our MWA dynamic spectrum (left panel of Fig. 4.3) instead of these two lanes, we have found more elaborate spectral and temporal structures in harmonic band. This is also evident from the panels in Fig. 4.5. Each panel corresponds to the cut across the central frequency of the regions marked in the left panel of Fig. 4.3 , and represents a plot of intensity vs. time. Each plot shows many small variations in intensity across time.

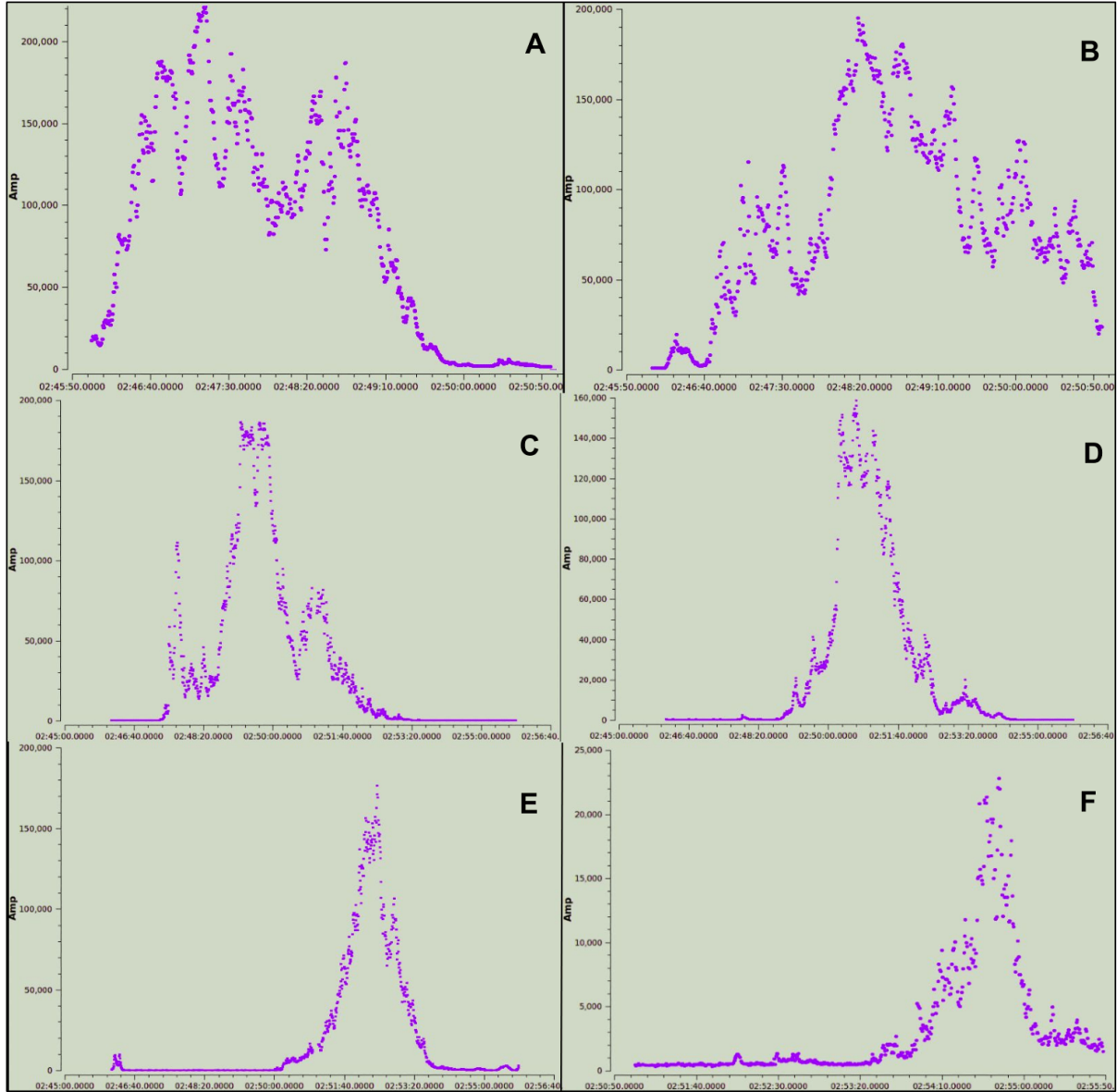


Figure 4.5: The different panels show cuts across time for the regions marked in left panel of Fig. 4.3. Conventionally, both F and H type II emission are believed to be organised in two bands of emission, coming from upstream and downstream, with respect to the shockfront. These panels highlight the fine temporal structure seen in the MWA data, suggesting that the phenomena is perhaps more complex than the conventional expectations.

Looking at these plots in Fig.4.5, we thought that these structures in harmonic emission might be coming from different locations on the bright compact source of the sun. Prior experience has shown that the compact burst sources are usually well modelled by an

elliptical Gaussian. To know if our assumption is correct or not, We have gotten some plots. To get these plots, we have used, CASA `imfit` task to fit an elliptic Gaussian over the brightest emission region on the optical disc of the sun. The plots show:

1. The shift of Right ascension(RA) and Declination(Dec) of the fitted Gaussian for different frequencies and time ranges in auto color scale (Fig.4.6).
2. RA and Dec shift for different frequencies and time ranges on the same color scale, to make is easier to track and compare the changes across all frequency bands (Fig.4.7).
3. Both fig.4.8 and fig.4.9 are showing half of the dynamic spectrum on which we have drawn arrows. The dynamic spectra show the amplitudes of the best fit Gaussian models. The direction of the arrows shows the direction towards which the Gaussian source has shifted with respect to a common origin, and the length of the arrow is proportional to the displacement of the best fit Gaussian model. The objective of the figure is to facilitate building a more complete picture of the physical phenomenon.
4. Error in RA and Dec of the fitted Gaussian for different frequencies and time ranges(Fig.4.10).
5. Peak amplitude of the fitted Gaussian and the error associated with it(Fig.4.11).
6. Major axis of the deconvolved image and the error associated with it(Fig.4.12).
7. Minor axis of the deconvolved image and the error associated with it(Fig.4.13).
8. Position angel(PA) of the deconvolved image and the error associated with it(Fig.4.14).
9. Major axis and minor axis of the fitted Gaussian in units of the PSF(Fig.4.15).
10. the PA difference between the fitted Gaussian and the PSF(4.16).

The y axis and x axis of all the panels of these figures represent frequency in MHz and time. Except, fig.4.6, all other figures have been obtained by using the same color scale for each plot of these figures. Before, we start discussing about the figures, we would like to point out why we think that all of these quantities obtained by Gaussian fitting are reliable. That's because the uncertainties in each of these quantities is small. In below there are some examples regarding this

- In fig. 4.10, each panel has two plots for error in RA and Dec of the fitted elliptic Gaussian. We can ignore all the brown structures in the plots as they fall outside of the harmonic emission band. It is evident that the error in all the plots fall between 18 to 3 arcsec.

- In fig.4.11, each panel describes the peak amplitude and the percentage error in the peak amplitude for the fitted Gaussian. If we compare the dynamic spectrum and the fitted amplitude plot for each panel, it is clear that we are able to capture the fine structures. Also the error in the fitted amplitude in all the panels falls below 6%.

This tells us that an elliptical Gaussian provides a good model for describing this time and frequency variable source. The reason we have used auto color scale in fig.4.6 to show the small scale changes in the plots, which were invisible in fig.4.7. To get fig.4.6 and fig.4.7, We have used the information about Right ascension(RA) and Declination(Dec) of the fitted Gaussian. We have obtained shift in RA and Dec by subtracting the values from the same reference in every panel. In our figures, the reference values were the RA and Dec value of the first time slice in the top left panel of the fig.4.6 or fig.4.7. In each panel of fig.4.6 fig.4.7, the top and bottom plot correspond to Dec shift and Ra shift in arcmin respectively. Below we would like to point out some things from fig.4.6, 4.7, 4.8 and 4.9:

1. In the top left panel of fig.4.6, the range of the Dec shift is from below -4.0 to above 2.4 and the range of the RA shift is from -3.6 to 1.2. Looking at the plots, it is apparent that there are continuous significant changes at least till 300 in the x-axis. This is also evident if we see the movement of the arrows on the dynamic spectrum (the top panel of fig.4.8). One more thing to note down is that these changes vary across the individual 2.5 MHz frequency bands.
2. The Dec and Ra shift in the top right panel of fig.4.6 ranges from 0.8 to -5.6 and -4.8, respectively. Here also if we look at the middle panel of fig.4.8, we can see changes in the length and the direction of the arrow. Especially, in the pink band of the harmonic emission band, where the arrows have become very small but if one looks at them carefully, then it is apparent that both of their magnitude and direction is changing across time and frequency.
3. In the middle left panel of fig.4.6, the deep blue patches in both plots are a physical and arise due to issues with the Gaussian fitting. The data corresponding to these points should be ignored in the following discussion. The red lane at the right end of both of the plots are coming from around 2 minutes after the harmonic emission happened. So if we ignore these values then most of the time the shift in the Dec and RA are ranging from 12 to around 3, and 16 to around 8. The missing regions in the lines of the arrow in the bottom panel of the fig.4.8 come from the previously mentioned blue patches. Here we can see the change in the length of the arrows in

the middle pink lane of the harmonic emission. Other than that region, the changes are so small that we are not able to observe in the arrows but we can see these changes in the graphs.

4. If we ignore the lane like structure at the end of both plots of the middle panel of fig.4.6, then the change of the RA and Dec shift ranges from 12 to 6 arcmin. Though it might look like from the plot of the Dec shift that after 300 in x-axis that the change became constant, but it is not the case, evident from the Dec shift plot of the middle panel of the fig.4.7. These changes are so small that it is not possible to see in the arrows (the top panel of the fig.4.9). But if one looks at the arrows carefully, then it can be seen that as the arrows cross the lane (a mixture of pink and red), the length slightly decreases.
5. The reddish orange structures at the left end of both plots of the bottom left panel of fig.4.6 are not coming from the harmonic emission region. So if we don't consider them, then the Dec shift spans from 10.5 to below 7.5 and the RA shift scales from 12 to 7.5. These changes are so small that we are not able to see them in the arrows in the middle plot of fig.4.9.
6. In the Dec shift plot of the bottom right panel, the region which extends from 200 to 400 in the x axis and from 79.6 to 79.1 in the frequency axis, looks like there has been no changes in the values. This is not the case if we look at the same plot in the bottom right panel of the fig.4.6. Again, we were not able to capture these small details in the arrows in the bottom panel of fig.4.6.

Looking at the above mentioned facts, it is very clear that there are systematic changes in the position of the fitted Gaussian across time and frequency.

We have already mentioned in the last chapter, that the deconvolved image gives us a sense of the actual sky image. Considering the source as a Gaussian, we have got the plots for major and minor axis and % error in both of the axes (fig.4.12 & 4.13). We can ignore the deep brown structures in these plots, as they are coming from outside of the harmonic emission band. If we look at these plots, it is obvious that the value of the major and minor axis is not constant across time. The range of the major axis and minor axis are around 700 to 350 arcsec and around 440 to 160 arcsec. Most of the time the errors in both of these values stay below 8 %.

These pieces of information tell us that the shape and orientation of the source is changing across time and frequency. Fig.4.14 describes the orientation of the best fit elliptical Gaussian, in other words the source. We can see that the position angle ranges from 180°

to 120 (ignoring the deep blue structures at the right and left end of the middle and bottom panels, respectively). The error associated with the PA in each of these panel falls below 10 degree.

Next we are interested to know how well our source is resolved.

So we have got major and minor axis in units of PSF(fig.4.15). Now if the source is a delta function,then we should get the values of major, minor axis close to 1. In our case (fig.4.15), the major axis varies from 1.80 to 1.05 and the minor axis spans from 1.65 to 1.05. This tells us that our region of interest is only marginally resolved. In the bottom panel of the fig.4.15, if we ignore the deep brown structures at the starting, then both values of major and minor axis stay close to 1.05. This implies that in these frequency channels, our compact emission region is barely resolved.

Another way to check if the source is resolved is to look at the PA difference between the convolved source and PSF. If we have a point source, then the PA difference should be close to 0 (or 180). It is evident from the plots that the PA difference stays away from 0 and 180. In fact, expect the bottom right panel, in all the plot, the value always falls between 70 to 130. In the bottom left plot, the region from 200 to 400 in the x-axis, which overlaps with the harmonic emission region, has the PA difference from 60 to 20.

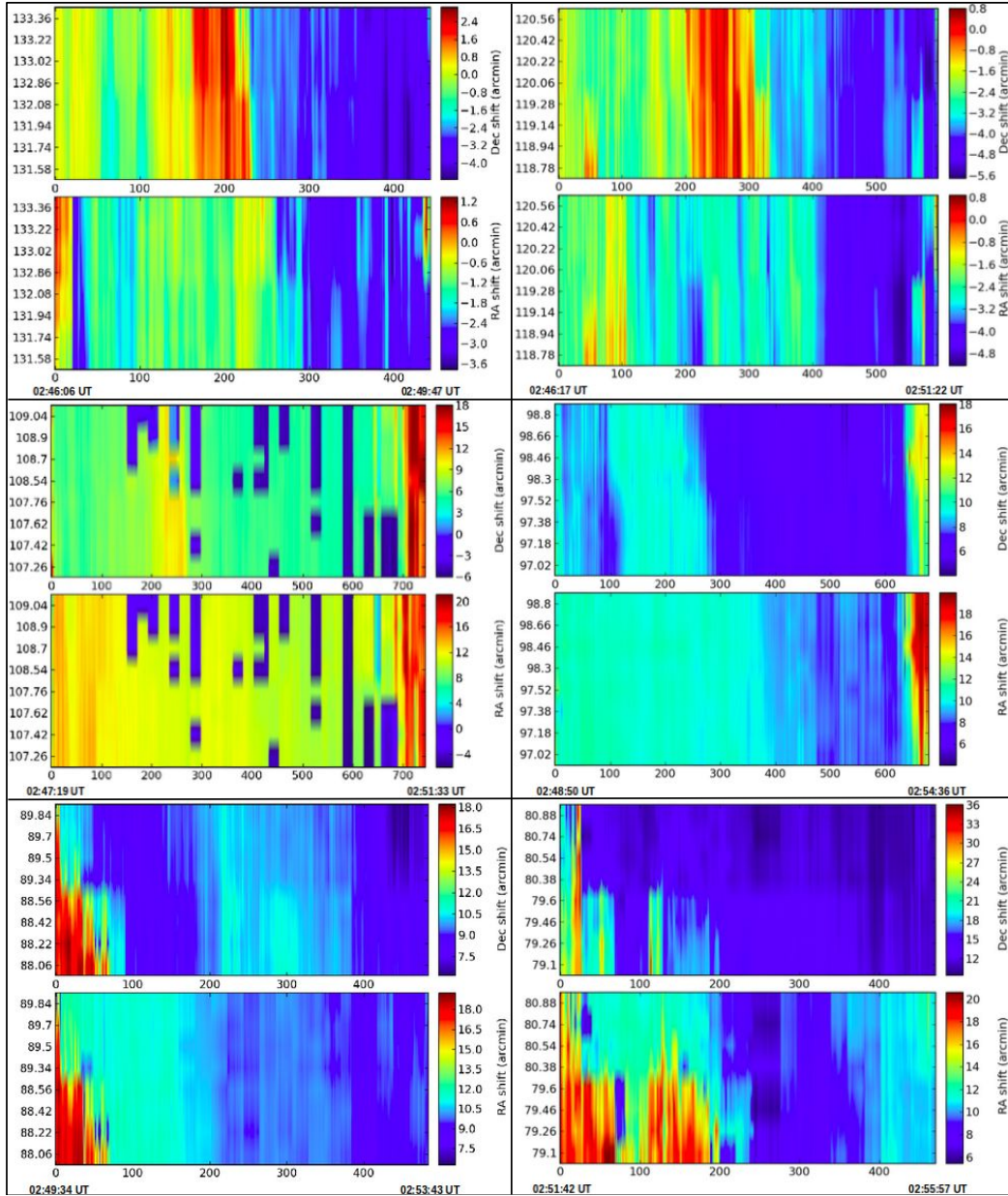


Figure 4.6: Each panel describes the shift of Right ascension(RA) and Declination(Dec) of the fitted Gaussian for different frequencies and time ranges. We suspect that the deep blue patches in the middle left panel are there due to something wrong with the data in those parts All the plots are on the auto color scale.

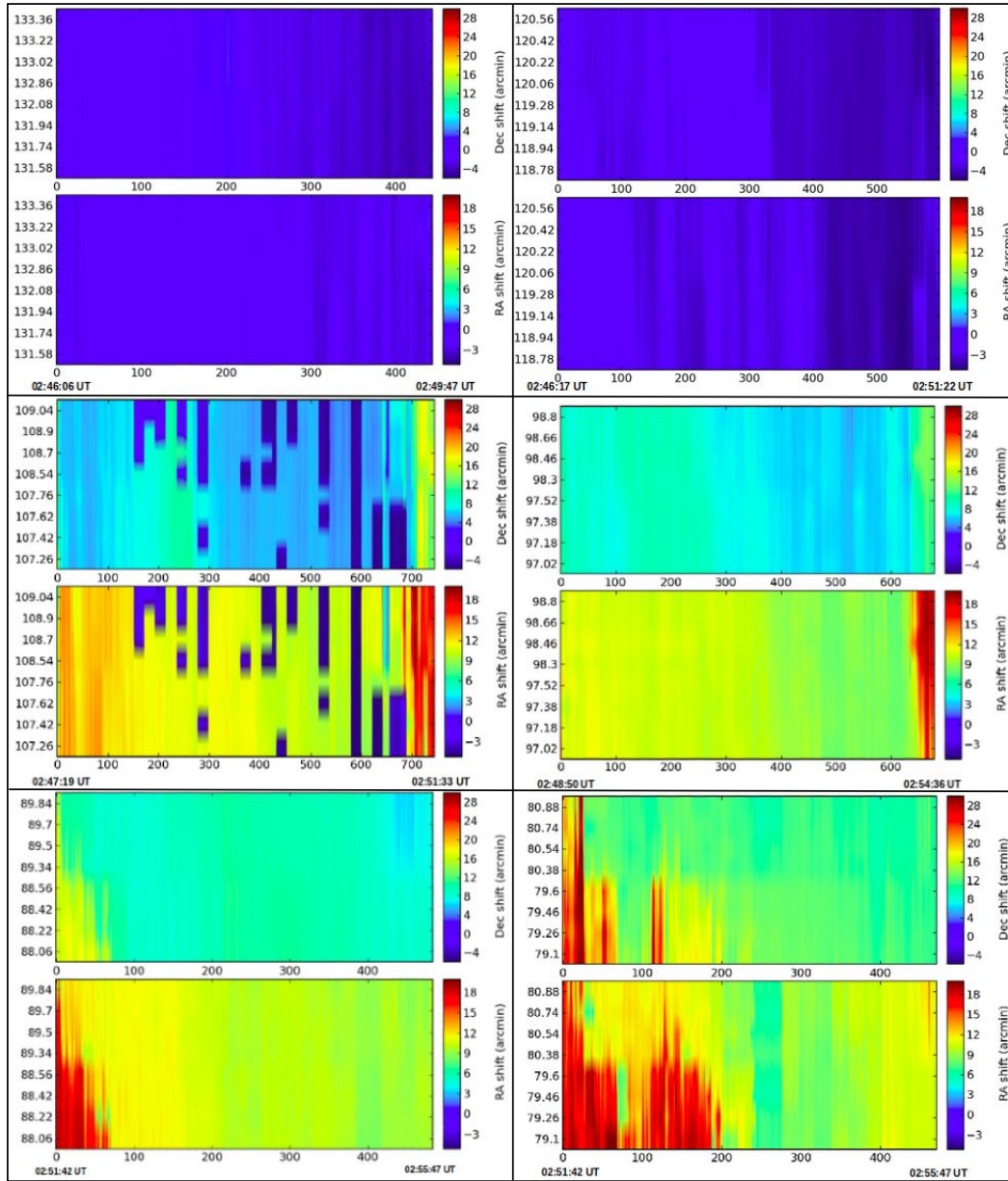


Figure 4.7: Each panel describes RA shift and Dec shift for different frequencies and time ranges in same color scale.

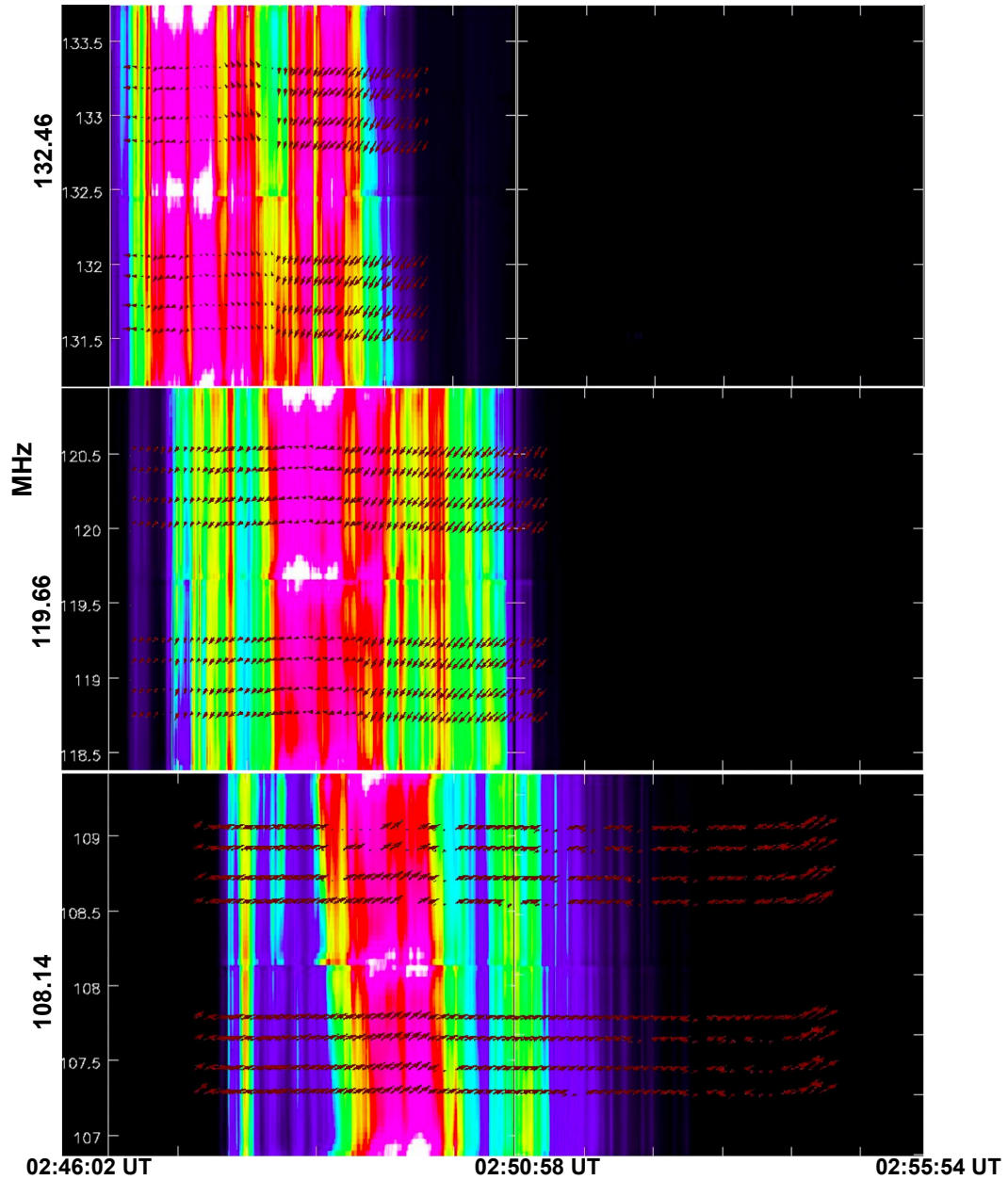


Figure 4.8: In each of the panel, we have drawn arrows on the dynamic spectrum. The starting point of the arrows is time and frequency, and the length and direction are shift in RA and Dec. This has been done to give a more visual representation of how the changes are happening across time and frequency.

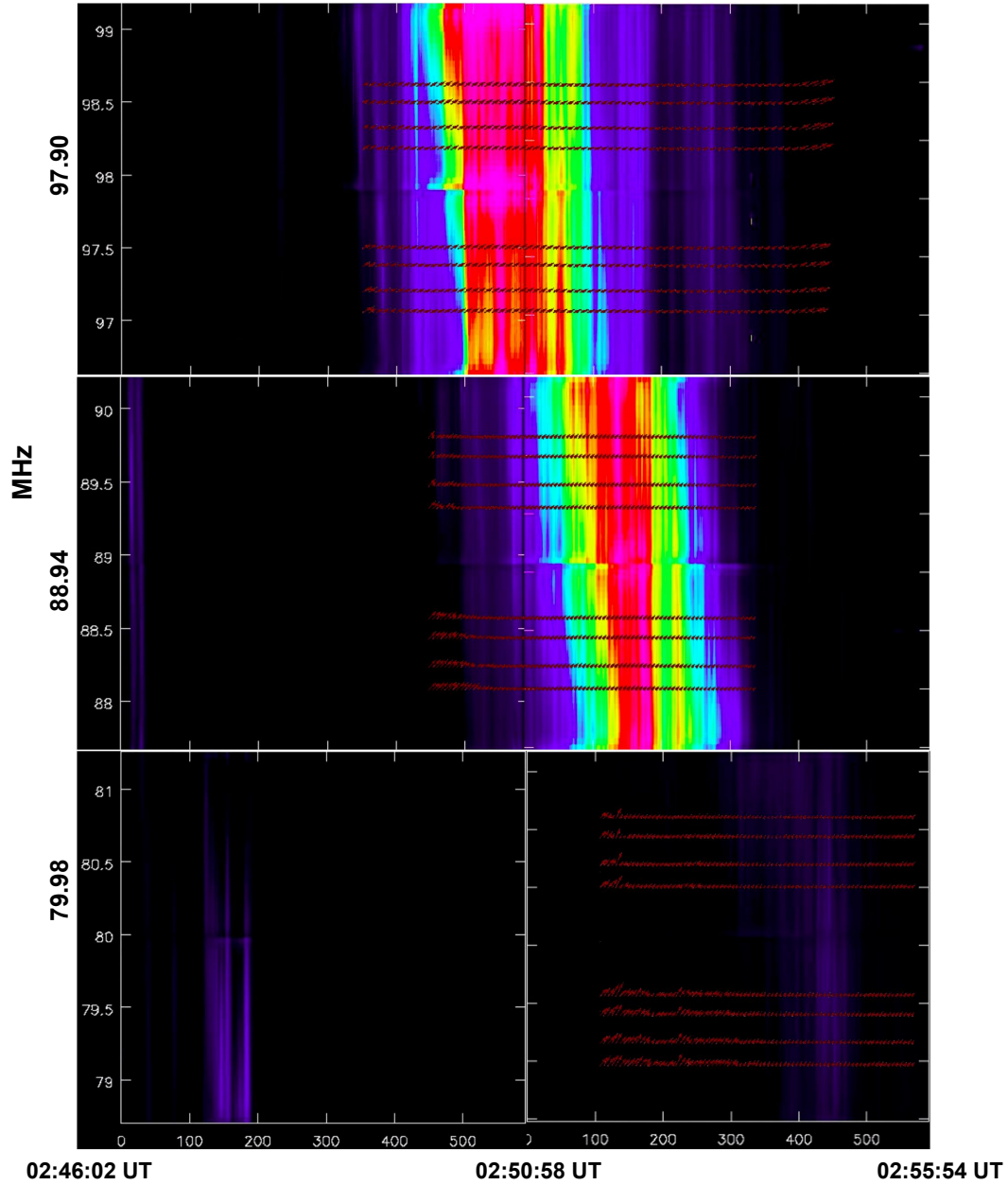


Figure 4.9: Looking at the panels, it seems like there no changes in the arrows across time and frequency, which is not the case. The changes in the RA and Dec shift are so small that it was not possible to capture in the arrow. One can look at the fig 4.6 or 4.7 to see these changes.

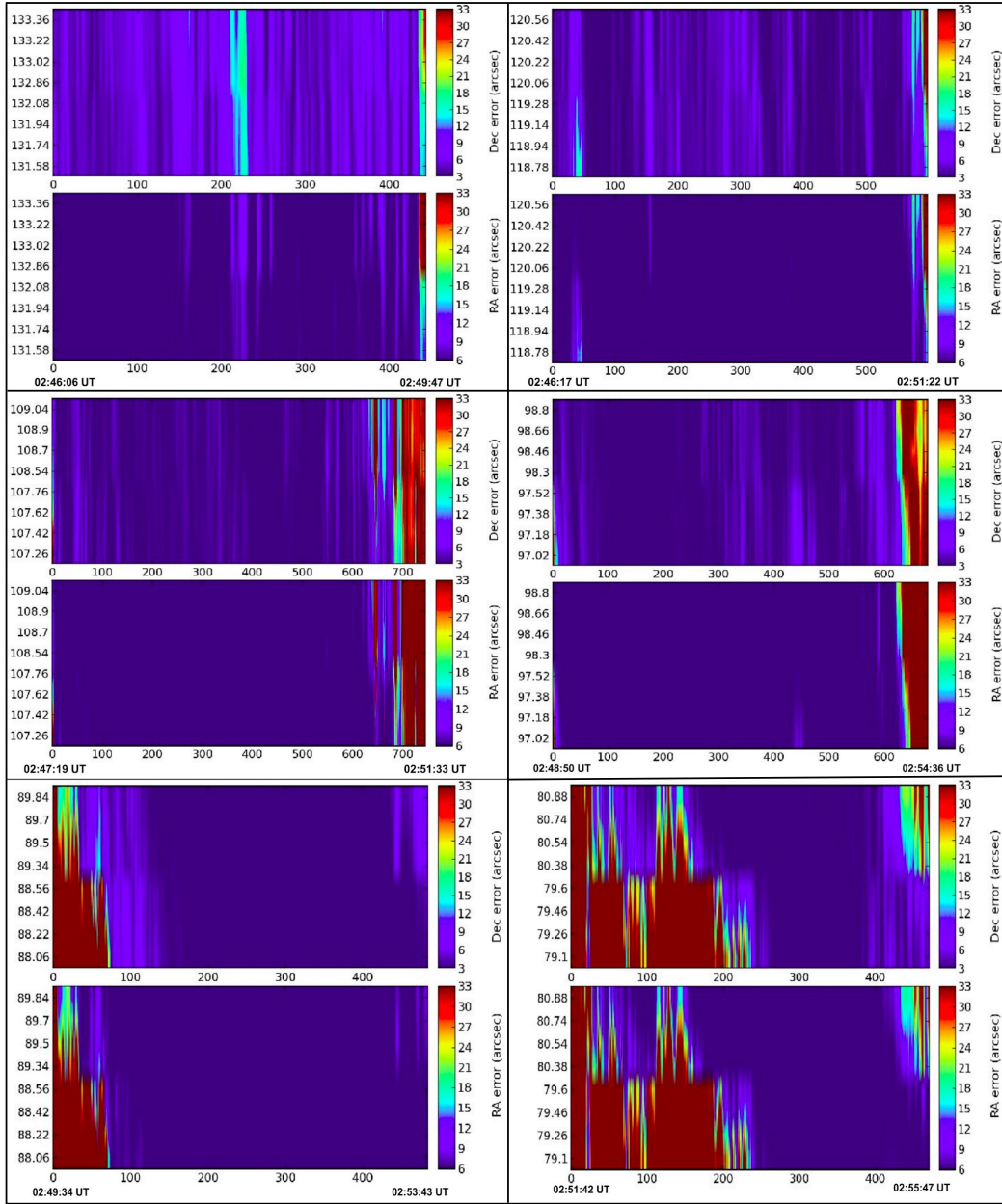


Figure 4.10: Each panel describes the error in RA and Dec of the fitted Gaussian for different frequencies and the time range. In each panel, most of the time the RA and Dec error fall below 12 arcsec, which is low. Because we have our RA and Dec shift in units of arcmin.

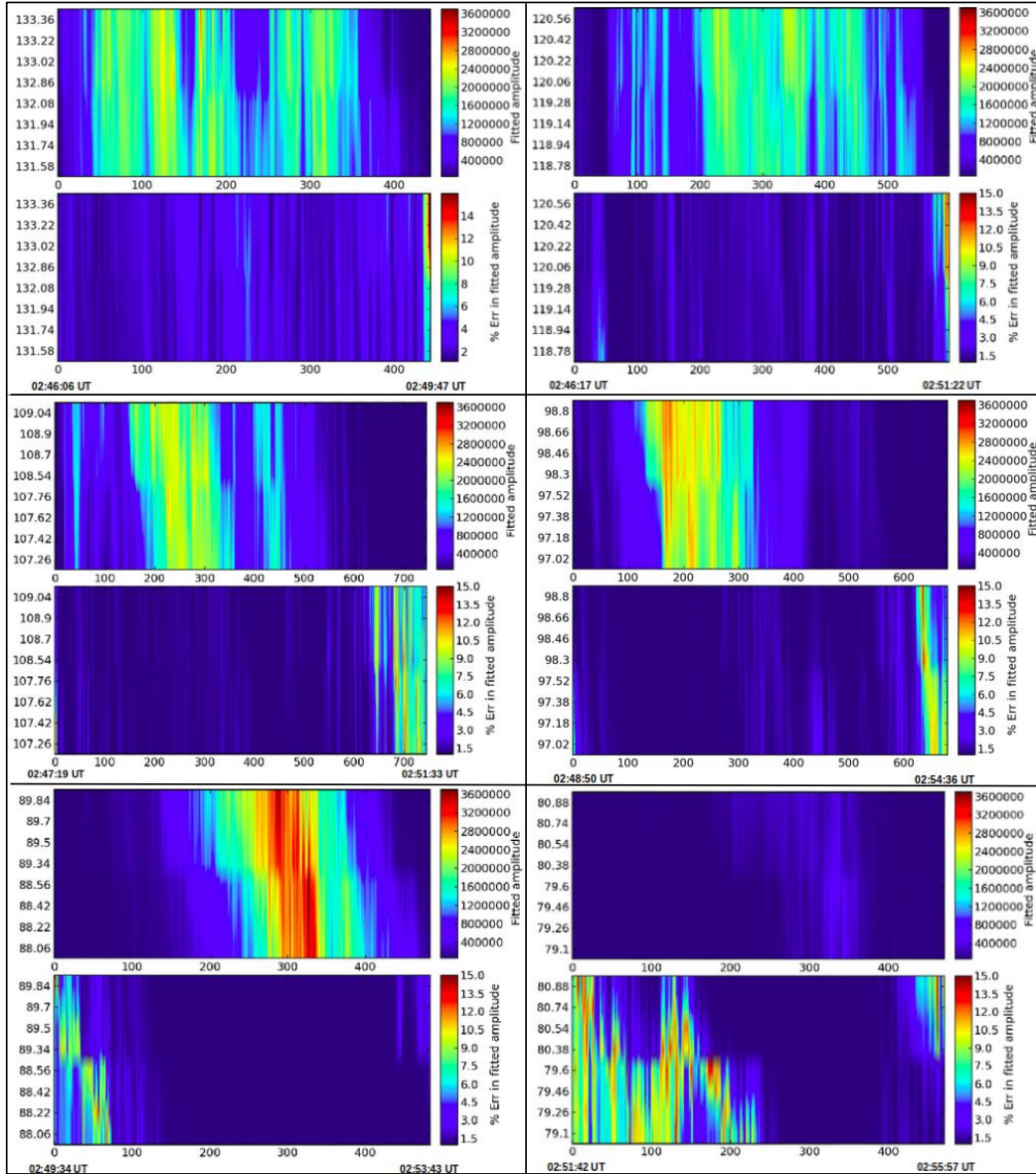


Figure 4.11: Each panel describes the value error in the peak amplitude of the fitted Gaussian for different frequencies and the time range. If we look at the dynamic spectrum and the plots of the peak amplitude, then it is evident that we are able to capture the fine structure in the harmonic emission band. Also the error for most of the time falls below 6 %. Looking at these facts we can say the Gaussian fitting was good.

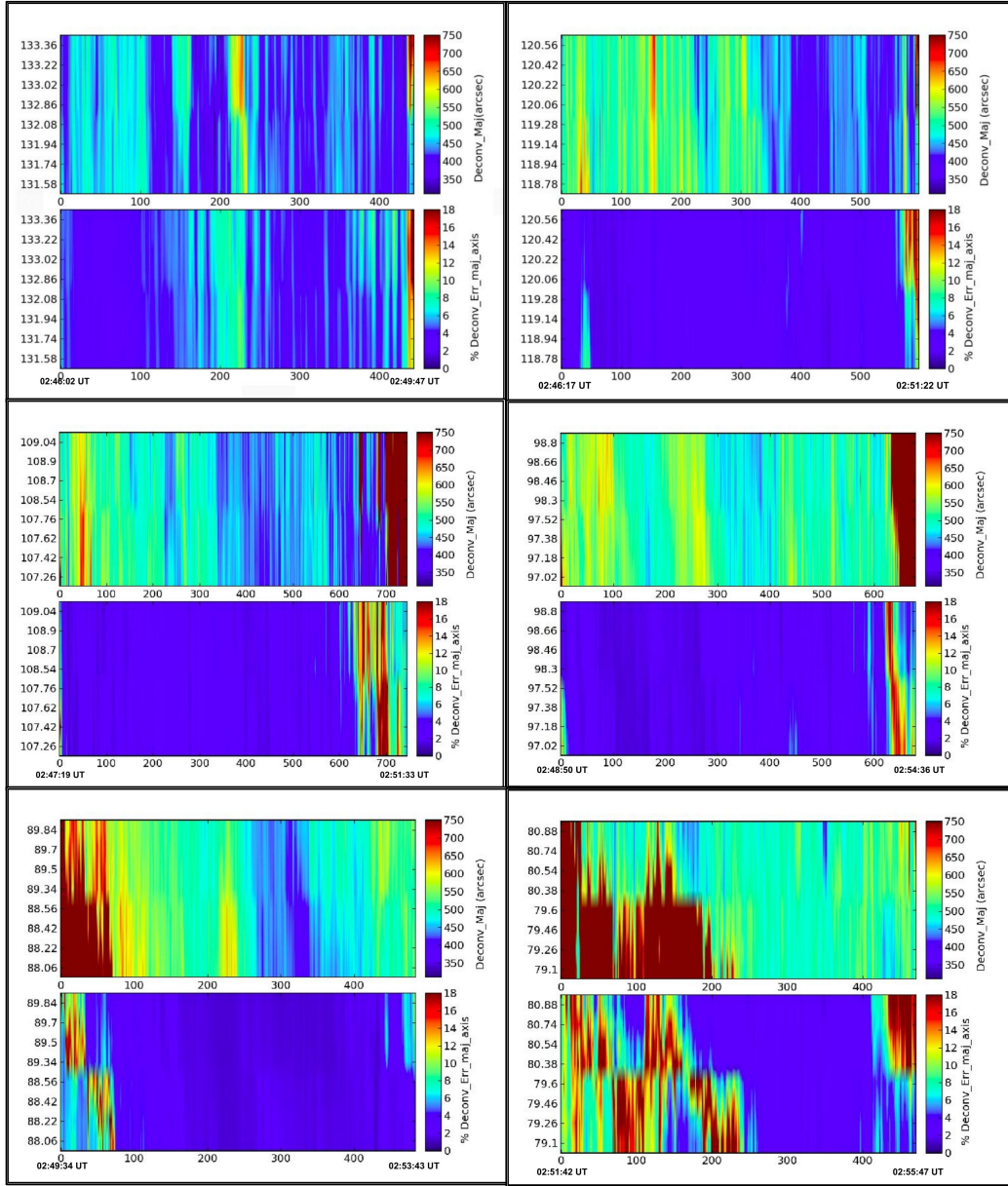


Figure 4.12: Each panel describes the value and the error in the major axis of the deconvolved image for different frequencies and the time range.

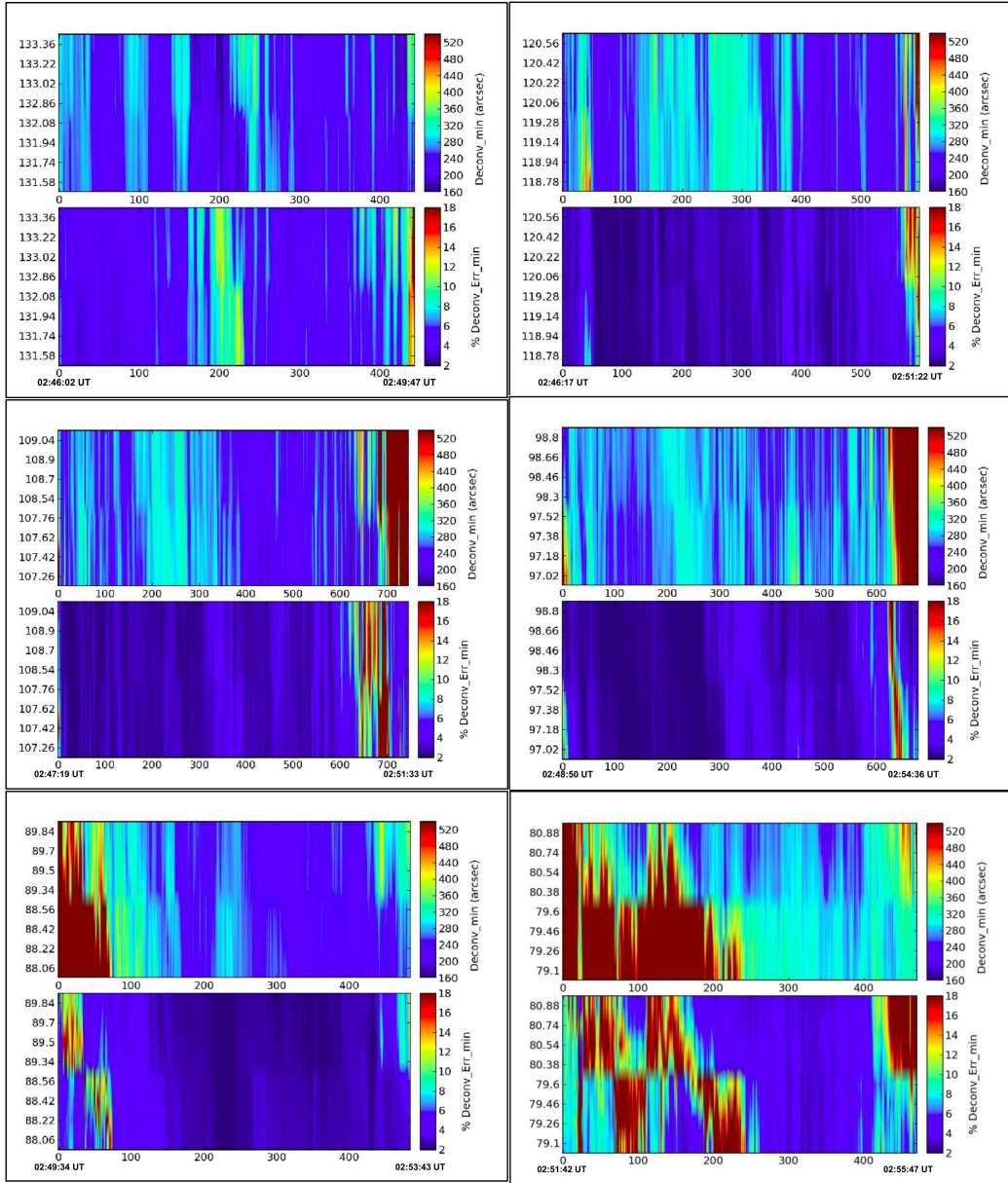


Figure 4.13: Each panel describes the value and error of the minor axis of the deconvolved image for different frequencies and the time range.

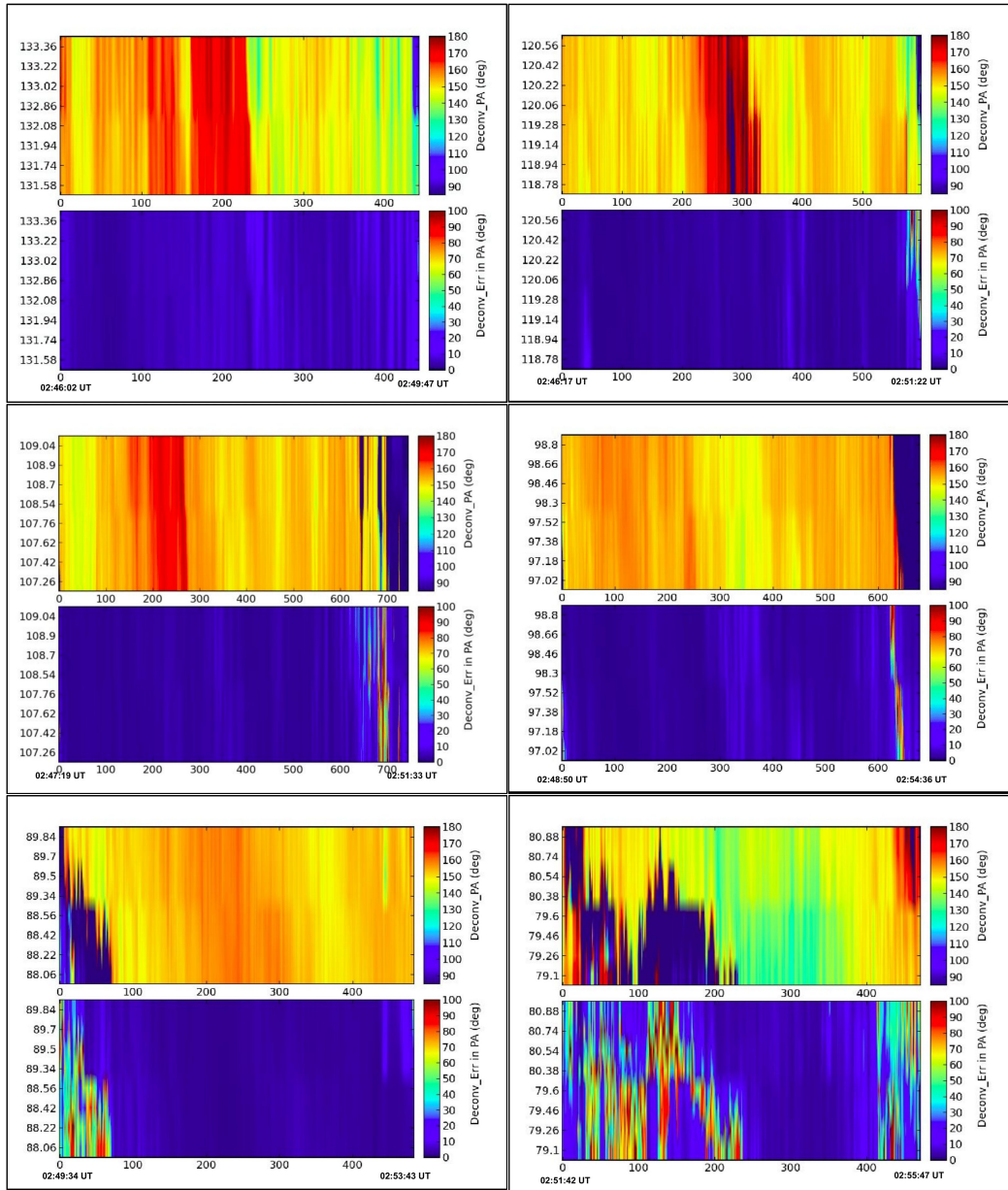


Figure 4.14: Each panel describes the value and error in the position angle(PA) of deconvolved image for different frequencies and the time range.

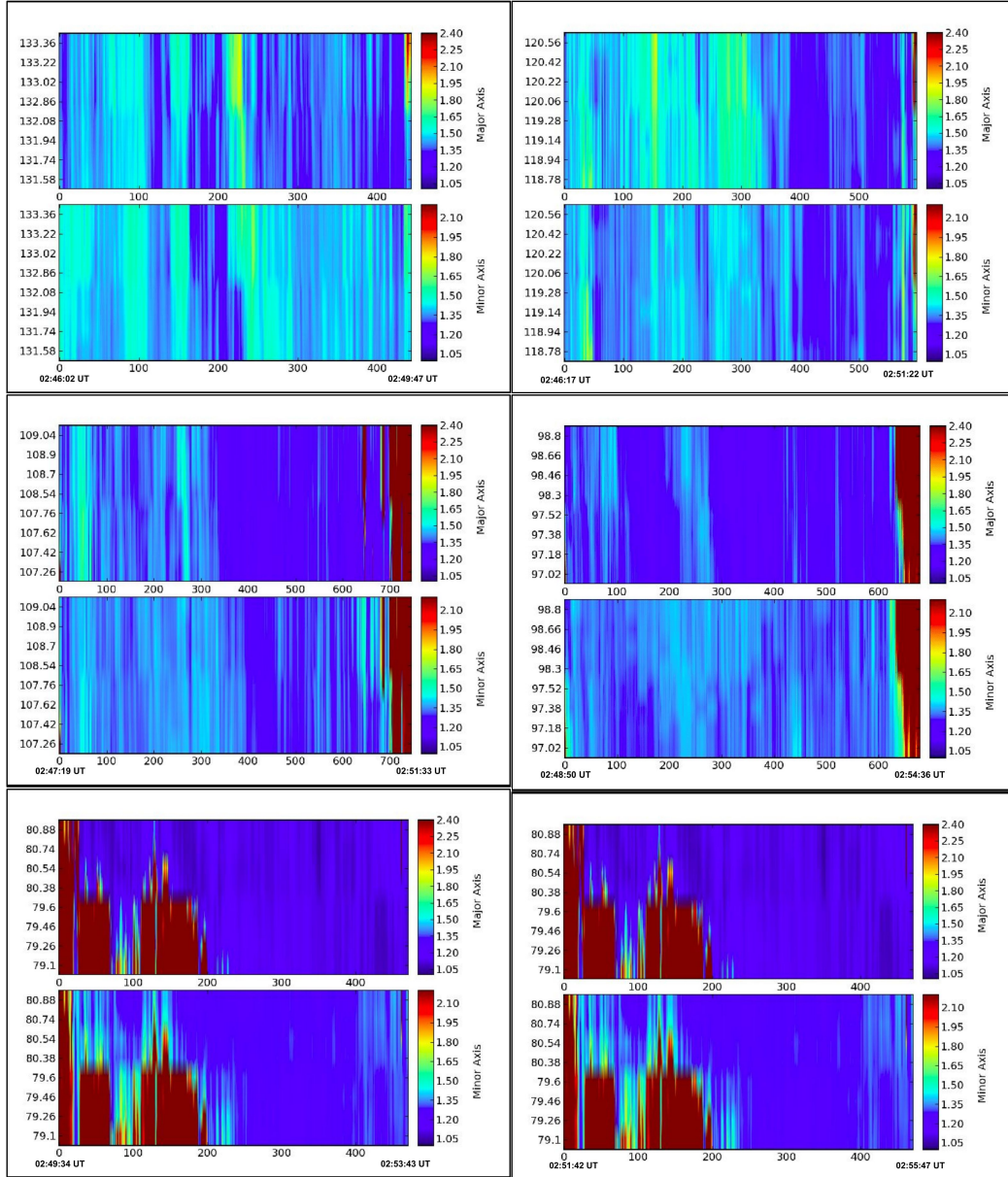


Figure 4.15: Each panel describes the major and minor axis of the convolved image in units of PSF for different frequencies and the time range

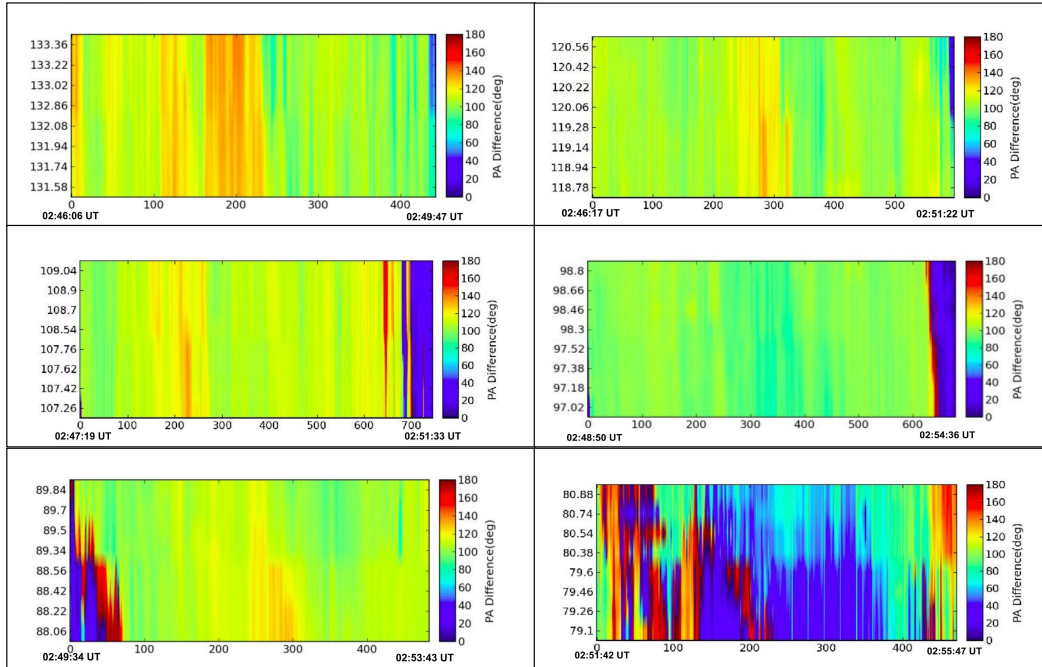


Figure 4.16: Each panel describes the PA difference between the convolved image and the PSF for different frequencies and the time range. This has been done to check how well our source has been resolved. In all the plots, the PA difference is well above 0, implying the source is resolved.

Chapter 5

Conclusion

This chapter briefly summarises the key aspects of the work done in thesis, the conclusions it lead to the directions for future work.

5.1 Development of a tool for exploring MWA solar data - SoLORM

As the MWA data is very voluminous and its analysis very computationally intensive, it is essential to have an efficient way of identifying interesting data to focus on. Building on prior work in this regard, we have developed SoLORM, to help the user to explore the MWA data, and identify interesting pieces of data based on user specified parameters. These parameters include measures of solar activity (e.g. sunspot number, 10.7 cm radio flux density) and events reported by other observatories (e.g. X-ray flares, CMEs, radio burts of type II and III etc.). We have also included geomagnetic indices- Kp & ap, to provide the user the information about how the various solar activities affect the near-Earth atmosphere. The program also makes it convenient to consult other useful sources of information like the SOHO LASCO CME catalogue for the month and `solarmonitor.org` webpage for the day on which the chosen event has taken place for the dataset of interest.

SoLORM was used to identify the M5.1 class flare which was associated with an interesting type II radio burst. The rest of this thesis was devoted to the analysis of this event. We

hope that this tool will be useful for other researchers who want to explore the MWA data and identify interesting pieces of data to work with.

5.2 Analysis of type II solar burst

The second half of my thesis work was devoted to imaging and analysing the type II radio burst associated with the M5.1 class flare. The various aspects of this work are briefly summarised. The bulk of the type II emission comes from the harmonic branch. There is a short duration at the very start of the event when the MWA data capture both the fundamental and the harmonic emissions.

5.2.1 Imaging and flux density calibration

Imaging was carried out using AIRCARS, an unsupervised imaging pipeline developed specifically for the MWA data. Imaging was done for 6 spectral bands spanning the range from 80–133 MHz. Each of these 6 spectral bands spans 2.5 MHz. Imaging was done with 0.5 s and 160 kHz time and frequency resolutions. Eight spectral channels were imaged for each of the 2.5 MHz bands, leading to more than 45,000 images. The quality of images was verified by organising these images into movies and their visual examination.

The usual flux density calibration do not work for the Sun. The solar signal is so strong that it needs to be attenuated to bring it within the operating range of the downstream electronics. Fortunately, we found Virgo-A in the very large field of view of MWA and made use of this opportunity to use it as a calibrator source. For this we used the information of the flux density spectrum of Virgo-A available from NASA/IPAC Extragalactic Database (NED) and a reliable model for the MWA primary beam available from Oberoi2017. Using this information, the scale factor by which the MWA radio maps have to be multiplied was determined, and the flux calibrated images were made.

5.2.2 Analysis of images

Visual inspection of a large number of images which had type II emission showed the presence of a compact burst source without any exception. It also turned out that the morphology of this source was described well by an elliptical Gaussian. This provided a convenient way to extract the properties of the burst emission. Each of the images which showed the presence of type II emission was fit with a Gaussian model with the following free parameters - position in the plane of the sky, amplitude, major and minor axes and orientation. Plots of each of these parameters and the uncertainties in them were made. The uncertainties in each of the parameters were carefully examined and it was confirmed that for all of the images for which type II emission was present, the uncertainties in the best fit parameters do not exceed a few percent. For orientation, we examined the difference between the orientation of the best fit Gaussian and the position angle of the PSF. For axial ratio, it was interesting to make the plots in units of the major and minor axes of the PSF. We also examined the variation in the location of the compact type II source as a function of time and frequency. All of these plots were presented in Chapter 4.

5.3 Results

Examination of these plots have lead to some interesting conclusions, which are enumerated below.

1. An early interesting finding was that the observed type II emission is much more complex in its morphology, as compared to the usual picture of fundamental and harmonic branches of emission, each of them further divided into two lanes of emission.
2. The type II emission is usually produced by magnetohydrodynamic (MHD) shock. For our case, this shock can be produced by flare or CME, which we need to investigate further. If the type II emission is produced from the shock front being driven by the CME propagating through the coronal medium, then because the CME itself is an extended structure, the shockfront is also should be extended. However, we find that the type II source is quite compact, suggesting that maybe the shock is

formed along only a small part of the CME front.

3. The type II source is found to be slightly resolved. Its major (minor) axis lies between 1.05–1.80 (1.05–1.65) in units of the PSF major (minor) axis. Also the difference between the position angles of the best fit Gaussian and the PSF is usually quite large. Thus the best fit Gaussian is not simply a scaled copy of the PSF. This implies that the measured source size is a true estimate of the apparent size of source, not a limitation of the instrumental resolution.
4. We know that the size of the PSF is proportional to λ . Hence, the fact that the best fit size of the type II, when measured in units of the size of the PSF, does not change much across the frequency range of 80–133 MHz, implies that the source size scales with λ . If the observed size of the source were to be dominated by scattering, it would also give rise to exactly the same scaling with λ . This suggests that the observed size of the source is indeed dominated by scattering, and the true size of the source must be even smaller.
5. An examination of the variation in the location of the type II source as a function of time and frequency shows that these variations are very systematic and very well correlated across neighbouring times and frequencies. The nature of these variations suggests that they are much more likely to arise due to a combination of scattering and refraction, than due to the physical motion of the shock location. If so, then it is conceivable that the correlation time scale of these variations will carry information about the time scale at which the medium is evolving and the bandwidth over which spectral correlation exists can be used to estimate the length scales of the structures giving rise to these variations.

5.4 Future Work

Here we briefly enumerate the directions, we believe, will be interesting to pursue in the future.

1. This thesis has focused on the type II radio emission associated with a M class X-ray flare. This event is very likely to be associated with emissions in other wave bands

and a CME, which we need to verify. It would be quite interesting to do a conventional multi-wavelength study of this event and try to build a detailed physical picture of this event.

2. As mentioned in the previous section, the size of the compact type II source seems to be governed by scattering. The details of the motion of the type II source in the plane of the sky, also suggest that it is dominated by scattering and refraction. So these data provide an excellent opportunity to use these observed properties of the source to constrain parameters of coronal turbulence. It seems feasible that the temporal correlation time scale of these source motions could contain information about the temporal scales at which the medium is evolving. Similarly the spectral correlation bandwidths of these source motions, assuming they can be determined using these data, might be helpful in constraining the spatial scales in the turbulent coronal medium.
3. Though only for a small part of the data, we have simultaneous observations of the both fundamental and the harmonic emission bands. In theory the fundamental and harmonic emission is believed to arise from the same shock-front at the same location. In practice the apparent sizes and locations of the sources at these frequencies are expected to be different due to the propagation effects involved. Having simultaneous imaging in these two bands is rather rare, and these data provide an excellent opportunity to explore the impact of propagation effects on this compact source of emission.

References

- [1] Markus J. Aschwanden. *Physics of the Solar Corona. An Introduction with Problems and Solutions (2nd edition)*. 2005.
- [2] A. Bhatnagar and W.C. Livingston. *Fundamentals of Solar Astronomy*. World Scientific series in astronomy and astrophysics. World Scientific, 2005.
- [3] Bin Chen et al. “Radio Spectroscopic Imaging of a Solar Flare Termination Shock: Split-band Feature as Evidence for Shock Compression”. In: *The Astrophysical Journal* 884.1 (2019), p. 63.
- [4] Jayaram N Chengalur, Yashwant Gupta, and K. S. Dwarkanath. *Low Frequency Radio Astronomy*. 2003.
- [5] J.J Condon and S. M. Ransom. *Essential Radio Astronomy*. 2010.
- [6] N. Jackson. “Principles of Interferometry”. In: *Jets from Young Stars II: Clues from High Angular Resolution Observations*. 2008, pp. 193–218.
- [7] Shubhendu Joardar. *Interferometry Aperture Synthesis And Radio Mapping*.
- [8] Surajit Mondal et al. “Unsupervised Generation of High Dynamic Range Solar Images: A Novel Algorithm for Self-calibration of Interferometry Data”. In: *The Astrophysical Journal* 875.2 (2019), p. 97.
- [9] Thomas L. Wilson, Kristen Rohlfs, and Susanne Hüttemeister. *Tools of Radio Astronomy*. 2009.